TUDelft

Delft University of Technology

Indirect evidence of Bi^{3+} valence change and dual role of Bi^{3+} in trapping electrons and holes for multimode X-ray imaging, anti-counterfeiting, and non-real-time force sensing

Lyu, Tianshuai; Dorenbos, Pieter; Wei, Zhanhua

Important note
To cite this publication, please use the final published version (if applicable).
Please check the document version above.

Full length article

Indirect evidence of Bi^{3+} valence change and dual role of Bi^{3+} in trapping electrons and holes for multimode X-ray imaging, anti-counterfeiting, and non-real-time force sensing

Tianshuai Lyu [a,*], Pieter Dorenbos [b], Zhanhua Wei [a,*]

[a] Xiamen Key Laboratory of Optoelectronic Materials and Advanced Manufacturing, Institute of Luminescent Materials and Information Displays, College of Materials Science and Engineering, Huaqiao University, Xiamen 361021, China
[b] Department of Radiation Science and Technology, Faculty of Applied Sciences, Section Luminescence Materials, Delft University of Technology, Mekelweg 15, Delft 2629 JB, the Netherlands

ABSTRACT

Discovering bismuth based smart materials that can respond to thermal, mechanical, and wide range X-ray to infrared photon excitation remains a challenge. Such materials have various uses like in advanced information encryption. In this work, valence state change between Bi^{2+}, Bi^{3+}, and Bi^{4+}, and the dual role of Bi^{3+} in trapping electrons and holes have been studied in Bi^{3+} or/and Ln^{3+} (Ln=Tb or Pr) doped $LiScGeO_4$ family of compounds by vacuum referred binding energy (VRBE) diagram construction, thermoluminescence, and spectroscopy. Electron release from Bi^{2+} has been evidenced. It can be used to experimentally determine the VRBE in the Bi^{2+} $^2P_{1/2}$ ground state and to realize Bi^{3+} negative quenching luminescence. Particularly, a new force induced charge carrier storage phenomenon has been discovered for non-real-time force recording. Wide range of emission tailorable afterglow, unique Bi^{3+} ultraviolet-A, white, and infrared afterglow have been demonstrated by using Bi^{3+} as a hole trapping and recombination center and using energy transfer processes from Bi^{3+} to Tb^{3+}, Pr^{3+}, Dy^{3+}, or Cr^{3+}. Proof-of-concept advanced anti-counterfeiting, information encryption, and X-ray imaging will be demonstrated. This work not only develops smart storage phosphors, but more importantly unravels the valence change between Bi^{2+}, Bi^{3+}, or Bi^{4+} and how it can affect the trapping and release of charge carriers with thermal, optical, or mechanical excitation. This work therefore can promote the discovery and development of Bi^{3+} based smart materials for various applications.

1. Introduction

A mechanoluminescence (ML) material is known as an inorganic compound which instantaneously emits photons during mechanical excitation [1–6]. Because of this feature, it has promising use in various fields [7–10], for instance in remote compression force distribution sensing [11], advanced anti-counterfeiting optical system [12], and structure damage inspection [13]. The best known ML materials are ZnS: Cu^+, Mn^{2+} [14] and $SrAl_2O_4$:Eu^{2+} [15]. For ML materials based applications, an expensive photomultiplier or complementary metal oxide semiconductor (CMOS) based light detector or camera has to be constantly used [16]. It is challenging to realize ML imaging since a mechanoluminescence process is generally transient and ML intensity is weak [17]. Particularly, a CMOS based flat panel detector has to be placed underneath a ML film for near-distance ML imaging [18]. The expensive panel detector can be easily damaged during mechanical excitation.

A new force induced charge carrier storage (FICS) phenomenon can be used for non-real-time force sensing and storage [19]. The FICS phenomenon was studied in Ref. [20]. It shows unique use to record an accidental moment like collision recording during vehicle accidents when mechanical excitation is transiently and randomly occurring. Few compounds are found to have the FICS phenomenon. In Ref. [20], ZnS: Cu^+ and $(Ba, Sr)Si_2O_2N_2$:Ln^{2+}, Dy^{3+} (Ln=Eu or Yb) with thermoluminescence (TL) glow bands in the temperature range from 280 to 600 K are reported. The trapping and de-trapping processes are not fully clear. For example, the effect of optical stimulation on the stored charge carriers by mechanical grinding is not known. Since the TL glow band is

---

* Corresponding authors.
E-mail addresses: lv_tianshuai@hqu.edu.cn, lv_tianshuai@126.com (T. Lyu), weizhanhua@hqu.edu.cn (Z. Wei).

close to room temperature (RT), the stored charge carriers generated during mechanical grinding rapidly fade at RT, leading to the loss of stored force information. Currently, it is unclear how to discover new compounds with the FICS phenomenon. The development of new alternatives then remains a challenge.

An afterglow or storage phosphor is known as an inorganic compound which stores free electrons and holes in traps after being irradiated by ionizing radiation like X-ray or γ-ray [21,22]. It has promising use in various fields like X-ray computed tomography (CT) [23], advanced anti-counterfeiting [24], dental radiographic imaging [25], advanced information encryption, and smart display [26]. The trapping and release processes of electrons and holes are crucial to understand how an afterglow or storage phosphor works [27]. Generally, there are many defects in compounds, which may act as electron or hole capturing centers [28]. Their energy level locations are often unknown. The transport processes of charge carriers are then difficult to discuss, resulting in a poor understanding of afterglow and storage phosphors [29–33]. This issue can be dealt with for lanthanide dopants with the chemical shift model that was developed in 2012 [34,35]. An improved version of the model was presented in Ref. [36]. It allows one to accurately determine vacuum referred binding energies (VRBEs) in the energy levels of different lanthanides in compounds like in Fig. 1 published in Ref. [37].

A short summary of white afterglow inorganic phosphors is provided in Table S1. There are rare reports on white and ultraviolet-A (315–400 nm) afterglow phosphors [38]. Ultraviolet-A afterglow has various uses like in photodynamic therapy and energy-saving catalysis [39]. White afterglow emission matches with the eye sensitivities of cone and rod retina cells. It means that the color of an object can be correctly emerged in the dark by using the white afterglow as an illumination source. This is a unique feature for developing illumination applications. There is interest to develop new white and ultraviolet-A afterglow phosphors.

Doping of bismuth into inorganic compounds appears an interesting strategy to discover new luminescent, storage, and mechanoluminescence materials [40–43], for example in $Cs_2Ag_{0.6}Na_{0.4}InCl_6$: Cr^{3+}, Bi^{3+} [44], $Bi_{1.5}ZnNb_{1.5}O_7$ [45], $LiScGeO_4$:Bi^{3+} [46], $Sr_3Sc_2Ge_3O_{12}$:Bi^{3+} [47], and $Ca_{1-x}Ba_xZnOS$:Bi^{3+} [48]. Bismuth has different valence states like Bi^{2+} and Bi^{3+} which show many electronic transitions [49]. It is often difficult to assign excitation bands. VRBE diagrams containing the

energy level locations of Bi^{2+} and Bi^{3+} are rarely reported until now. Deep and convincing understanding on luminescence mechanism, trapping, and de-trapping processes of electrons and holes still remains a challenge. Particularly, the valence state change between Bi^{2+}, Bi^{3+}, or Bi^{4+} is still not fully clear. More than 120 h ultraviolet-A persistent luminescence was claimed in Bi^{3+} doped $LiScGeO_4$ after 254 nm UV-light charging [46,50]. It means that $LiScGeO_4$ with many defect(s) is a promising compound to develop new afterglow or storage phosphors. However, the nature of defects in Bi^{3+} doped $LiScGeO_4$ still remains unknown. To solve this problem, photoluminescence excitation and emission spectra of Bi^{3+}, Tb^{3+}, or Pr^{3+}-doped $LiScGeO_4$ and of the undoped host were investigated at 10 K in a recent case study in Ref. [37]. Results are utilized to establish the VRBE diagram of $LiScGeO_4$ including the energy level locations of Bi^{3+} and different lanthanides. It is partly shown in Fig. 1. Based on this VRBE diagram, Eu^{3+} was evidenced as a shallow electron trap and Bi^{3+}, Pr^{3+}, and Tb^{3+} co-dopants acted as stable hole traps in $LiScGeO_4$. Good charge storage properties were demonstrated where upon recombination the electron liberated from Eu^{2+} transports via the conduction band to recombine with either Bi^{4+}, Pr^{4+}, or Tb^{4+} to generate Bi^{3+}, Pr^{3+}, or Tb^{3+} recombination emission. In the VRBE diagram in Fig. 1, Bi^{3+} is predicted to act as a 0.74 $\pm$0.5 eV shallow electron trapping center. However, the real VRBE in the Bi^{2+} $^2P_{1/2}$ ground state in $LiScGeO_4$ remains unknown. Particularly, how to engineer Bi^{2+} electron trapping depth in Bi^{3+} doped $LiScGeO_4$ for developing new afterglow and storage phosphors is still not known. The same applies to Bi^{3+} doped $LiTaO_3$ [51]. $LiScGeO_4$ and $LiLuGeO_4$ have the same crystal structure but with slightly different VRBE in the conduction band. A thermoluminescence study of Bi^{3+} doped $LiSc_{1-x}Lu_x$-GeO_4 solid solutions will be helpful to determine the VRBE in the Bi^{2+} $^2P_{1/2}$ ground state. Moreover, the valence state change between Bi^{2+}, Bi^{3+}, or Bi^{4+} is not evidenced and the FICS phenomenon has not yet been reported in Bi^{3+} or/and Ln^{3+} (Ln=Tb or Pr) doped $LiScGeO_4$ family of compounds.

In this work, the valence state change between Bi^{2+}, Bi^{3+}, and Bi^{4+} after illumination by 254 nm or 365 nm of different duration has been evidenced in the $LiScGeO_4$ family of compounds by utilizing the VRBE diagram, thermoluminescence, and spectroscopy. Electron liberation from Bi^{2+} to recombine with holes captured at Bi^{4+}, Tb^{4+}, or Pr^{4+} has been demonstrated in Bi^{3+} or/and Ln^{3+} doped $LiScGeO_4$ and $LiLuGeO_4$.
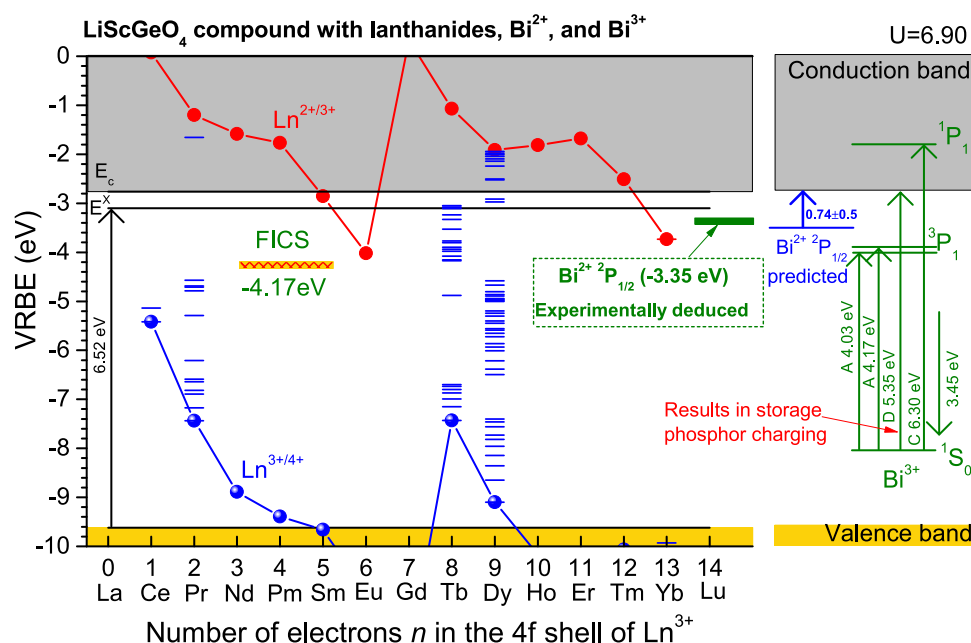

Fig. 1. Vacuum referred binding energy (VRBE) diagram for the $LiScGeO_4$ compound. The VRBE level locations of Bi^{2+}, Bi^{3+}, and different lanthanides are provided. A comparison of the VRBE in the predicted and experimentally deduced Bi^{2+} $^2P_{1/2}$ ground state is shown.

Based on this result, the VRBE in the Bi^{2+} $^2P_{1/2}$ ground state has been experimentally determined to be ~−3.35 eV for $LiScGeO_4$ and $LiLuGeO_4$. Proof-of-concept Bi^{3+} negative quenching luminescence has been demonstrated by using electron liberation from Bi^{2+}.

Particularly, a new force induced charge carrier storage (FICS) phenomenon has been demonstrated in Bi^{3+} or/and Ln^{3+} doped $LiScGeO_4$ family of compounds. The stored charge carriers created by the FICS effect can be liberated by wide range of 365 to 656 nm laser. The FICS effect has promising use in non-real-time force storage and sensing application. To develop emission-tailorable phosphors with unique white and infrared afterglow for anti-counterfeiting application, Dy^{3+} and Cr^{3+} are co-doped with Bi^{3+} by exploiting energy transfer processes. Wide range of emission tailorable afterglow, unique Bi^{3+} UVA afterglow, and white afterglow have been demonstrated by using Bi^{3+} as a hole trapping, recombination center, and energy transfer processes from Bi^{3+} to Tb^{3+}, Pr^{3+}, Dy^{3+}, or Cr^{3+}. Proof-of-concept advanced anti-counterfeiting, information encryption, and X-ray imaging have been demonstrated by using the developed Bi^{3+} or/and Ln^{3+} doped $LiScGeO_4$ family of compounds. This work not only reports smart storage phosphors, but more importantly unravels the valence change between Bi^{2+}, Bi^{3+}, or Bi^{4+} and how it can affect the trapping and release of charge carriers with thermal, optical, or mechanical excitation. This work therefore can promote the discovery and development of Bi^{3+} based smart materials for various applications.

2. Experimental

The starting Li_2CO_3 material with a high purity of 4 N (99.99%) was bought from the Shanghai Makclin Biochemical company. The other starting materials (99.99%) were purchased from the Shanghai Aladdin Biochemical Technology company. Bi^{3+}, Cr^{3+}, and different lanthanides doped $LiSc_{1-x}Lu_xGeO_4$ ($x = 0$ until 1) compounds were synthesized with a high temperature solid-state reaction method. Li^+ partly volatilizes at high temperature during synthesis. More than 10% Li^+ above its stoichiometric ratio in $LiSc_{1-x}Lu_xGeO_4$ was then utilized. The masses of the utilized dopants have been determined by molar ratios of dopants to a compound host composition. Based on the compound compositions like $LiSc_{0.25}Lu_{0.75}GeO_4$:$0.005Bi^{3+}$, appropriate chemicals of Li_2CO_3 (99.99%), Sc_2O_3 (99.99%), Lu_2O_3 (99.99%), GeO_2 (99.99%), Bi_2O_3 (99.99%), Cr_2O_3 (99.99%), Pr_6O_{11} (99.99%), Tb_4O_7 (99.99%), Dy_2O_3 (99.99%), or CeF_3 (99.99%) were weighted and then well mixed in an agate mortar with the help of a pestle and ethanol solution. The milled chemicals were placed in a covered corundum crucible. They were kept first at 800 °C for 2 h and then at 1150 °C for 10 h in a tube furnace under ambient atmosphere. A heating rate of 3 °C/min was used for the tube furnace. After cooling to RT (~298 K), the synthesized compounds were ground prior to further measurements. To explore anti-counterfeiting application, $LiTaO_3$:$0.005Bi^{3+}$, $0.002Dy^{3+}$ with afterglow and photochromic features and Cs_2ZrCl_6:$0.01Sb^{3+}$ perovskite crystals with intense photoluminescence upon 254 or 365 nm excitation have been synthesized by the methods in Refs. [52,53].

The structures of the synthesized $LiSc_{1-x}Lu_xGeO_4$ compounds were first identified with a Japan Rigaku SmartLa X-ray diffraction setup. Transmission electron microscope (TEM) photograph and energy dispersive X-ray (EDX) mapping were recorded by a FEI Talos F200X G2 (Enfinium SE 976) facility. X-ray excited emission spectra as a function of time at 100 K were measured by a setup which consists of a cryostat, a QE65000 spectrometer (Ocean Optics), and a MOXTEK TUB00083–2 X-ray tube that is operated at 45 kV, 70 μA, and 3.15 W. For X-ray excited scintillation light yield comparison, X-ray excited emission spectra at RT were recorded by a Edinburgh FLS980 spectrometer together with a TUB00154–9I-W06 X-ray tube (MOXTEK, Ltd.) which is operated at 60 kV, 200 μA, and 12 W. The photoluminescence excitation (PLE) spectrum (λ_{em}=358 nm) of $LiSc_{0.25}Lu_{0.75}GeO_4$:$0.005Bi^{3+}$ at 10 K and photoluminescence emission (PL) spectra of $LiScGeO_4$:$0.005Bi^{3+}$ in the temperature range from 10 to 310 K were measured with the 4B8 VUV

spectroscopy station at Beijing Synchrotron Radiation Facility (BSRF).

Above 200 nm PLE and PL spectra, fluorescence decay curves, and RT isothermal decay spectra or curves after a Hg lamp (254 nm UV-light) or different energy photon illumination were measured in the dark by a Edinburgh FLS1000 spectrometer. The PLE spectra were corrected by wavelength dependent intensities of the used xenon lamp. The PL spectra were corrected by the wavelength dependent detection quantum efficiencies of the utilized photomultipliers in the FLS1000 spectrometer. Thermoluminescence (TL) emission (TLEM) spectra, TL glow curves, RT isothermal decay curves, optically stimulated luminescence, and X-ray excited integrated emission intensities from ~300 to 750 nm were measured by a setup. It combines a cryostat operated in the temperature range from 100 to 600 K, a heater operated in the temperature range from RT (~298 K) to 773 K, a Hamamatsu R928P photomultiplier (PMT), a shutter, a Hg lamp (254 nm UV-light, ~300 μW/cm²), a 365 nm UV-lamp (~400 μW/cm²), a commercial white light-emitting diode (WLED) lamp (~60 mW/cm²), a 656 nm laser emitting diode (~8 mW/cm²), and a MOXTEK TUB00083–2 X-ray tube. The dose rate of the X-ray tube operated at 30 kV, 50 μA, and 1.5 W is ~0.5 Gy/min. For above RT TL comparison, the X-ray exposure duration is fixed at 200 s and a constant sample mass of ~0.0300 g has been used for all samples. Prior to TL measurements, samples have been heated to 723 K at a heating rate of 1 K/s and then kept at 723 K for 180 s in order to release randomly stored charge carriers in traps. The above RT TL intensities are comparable since they are recorded by a same setup with a same configuration.
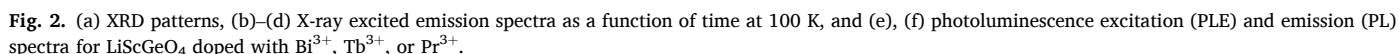
3. Results

3.1. Demonstrating Bi^{3+} valence state change with spectroscopy in Bi^{3+} co-doped $LiSc_{1-x}Lu_xGeO_4$

Fig. 2(a) presents the X-ray diffraction (XRD) patterns for the synthesized Bi^{3+} or/and lanthanides doped $LiScGeO_4$. All the prepared compounds are of single phase since their XRD patterns are consistent with the $LiScGeO_4$ reference card (PDF#78–1327). The similar applies to Bi^{3+} or/and lanthanides doped $LiLuGeO_4$ in Fig. S2.

In Ref. [37], we studied Eu^{3+} doping acting as shallow e-trap and with Bi^{3+}, Tb^{3+}, or Pr^{3+} as deep hole traps. In this work, we focus on Bi^{3+} as shallow e-trap co-doped with Tb^{3+} or Pr^{3+} as deep hole traps where Bi^{3+} can also act as deep hole trap. In addition, Dy^{3+} or Cr^{3+} was used as co-dopants with the aim to change the emission color by exploiting energy transfer processes with Bi^{3+}.

To unravel the luminescence nature, Bi^{3+}, Cr^{3+}, and/or lanthanides doped $LiSc_{1-x}Lu_xGeO_4$ family of compounds are first studied. Fig. 2(b) shows the continuous X-ray excited emission spectra of $LiScGeO_4$:$0.003Bi^{3+}$ as a function of time at 100 K. 100 K was selected because the nature of emissions can be better distinguished at 100 K compared with at RT. The emission spectrum is composed of a weak Bi^{3+} $^3P_1\rightarrow^1S_0$ emission band peaked at ~362 nm and a broad emission band peaked at ~540 nm attributed to the intense host exciton emission (E^{ex}) [37]. Fig. 2(c) presents the continuous X-ray excited emission spectra of $LiScGeO_4$:$0.005Pr^{3+}$ at 100 K. The emission spectrum shows the host exciton emission (E^{ex}) and the typical Pr^{3+} 4f→4f emission lines. Fig. 2(d) shows the X-ray excited emission spectra of $LiSc_{0.25}Lu_{0.75}GeO_4$:$0.005Bi^{3+}$, $0.002Tb^{3+}$, $0.004Pr^{3+}$ as a function of time at 100 K. The emission spectrum shows the host exciton emission (E^{ex}), the Bi^{3+} $^3P_1\rightarrow^1S_0$, and characteristic 4f→4f emission lines of both Tb^{3+} and Pr^{3+}.

Fig. 2(e) shows the photoluminescence excitation (PLE) and emission (PL) spectra of $LiScGeO_4$:$0.005Bi^{3+}$, $0.005Tb^{3+}$ recorded at RT. Upon 250 or 288 nm excitation, both the Bi^{3+} $^3P_1\rightarrow^1S_0$ and the Tb^{3+} $^5D_4\rightarrow^7F_j$ emissions emerge. Monitored at the Bi^{3+} emission at 360 nm, the PLE spectrum is composed of the Bi^{3+} excitation D-band peaked at ~230 nm and the Jahn-Teller split Bi^{3+} $^1S_0\rightarrow^3P_1$ excitation bands peaked at about 297 and 307 nm [54]. Monitored at the Tb^{3+} typical emission at 552 nm, not only the intrinsic Tb^{3+} excitation bands peaked at 250 and 266 nm

Fig. 2. (a) XRD patterns, (b)–(d) X-ray excited emission spectra as a function of time at 100 K, and (e), (f) photoluminescence excitation (PLE) and emission (PL) spectra for LiScGeO$_4$ doped with Bi^{3+}, Tb^{3+}, or Pr^{3+}.

appear, but also both the Bi^{3+} excitation D-band and the A-band are observed. It means that there is an energy transfer process from Bi^{3+} to Tb^{3+} in LiScGeO$_4$:0.005Bi^{3+}, 0.005Tb^{3+}. Figs. 2(f) and S23 show the PLE and PL spectra of LiScGeO$_4$:0.003Bi^{3+}, 0.005Pr^{3+}, LiScGeO$_4$: 0.003Bi^{3+}, 0.005Dy^{3+}, and LiScGeO$_4$:0.005Bi^{3+}, 0.005Cr^{3+}. Like LiScGeO$_4$:0.005Bi^{3+}, 0.005Tb^{3+} in Fig. 2(e), the common Bi^{3+} excitation D-band and A-band also emerge in the PLE spectra in Fig. S23 when the typical Dy^{3+} or Cr^{3+} emissions are monitored at 580 or 1100 nm [55, 56]. It implies that there are energy transfer processes from Bi^{3+} to Dy^{3+} or Cr^{3+}, respectively.

Fig. 3(a) shows the PLE and PL spectra of LiScGeO$_4$:0.003Bi^{3+}. Upon 296 nm excitation, a broad emission band peaked near 354 nm appears. Like in Ref. [37,50,57–59], it is attributed to the Bi^{3+} $^3P_1 \rightarrow {}^1S_0$ transition. Monitored at 360 nm, the PLE spectrum is composed of an excitation band peaked at ~231 nm and two excitation bands peaked at ~296 and ~306 nm. Different than that in Ref. [50], the excitation band peaked at ~231 nm is newly observed, which is attributed to charge transfer from Bi^{3+} to the conduction band (CB) of LiScGeO$_4$, i.e., the Bi^{3+} D-band. The excitation bands peaked at ~296 and ~306 nm are attributed to the Jahn-Teller split Bi^{3+} $^1S_0 \rightarrow {}^3P_1$ excitation [60–62].

To unravel the luminescence nature of bismuth, Bi^{3+} single doped LiSc$_{1-x}$Lu$_x$GeO$_4$ family of compounds are studied. Fig. 3(b) and 3(c) present the PL (λ_{ex}=290 nm) and PLE (λ_{em}=350 nm) spectra for LiSc$_{1-x}$Lu$_x$GeO$_4$:0.005Bi^{3+}. With increasing x, ~5 nm blue-shift emerges in the Bi^{3+} $^3P_1 \rightarrow {}^1S_0$ emission band. The Bi^{3+} excitation A-band remains stationary, while about 4 nm red-shift appears in the Bi^{3+} excitation D-band.

Fig. 3(d) compares the photoluminescence excitation (PLE, λ_{em}=358 nm) spectrum at 10 K and the thermoluminescence excitation (TLE) curve for the LiSc$_{0.25}$Lu$_{0.75}$GeO$_4$:0.005Bi^{3+} which is a representative solid solution for the prepared LiSc$_{1-x}$Lu$_x$GeO$_4$ family of compounds. It indicates that traps can be filled through the Bi^{3+} D-band excitation.

To study the valence state change of Bi^{3+}, PLE and PL spectra after

254 nm UV-light illumination in the dark were recorded. Fig. 3(e) and (f) show the PLE spectra (λ_{em}=360 nm) for LiSc$_{0.25}$Lu$_{0.75}$GeO$_4$:0.005Bi^{3+} and LiScGeO$_4$:0.003Bi^{3+} after being illuminated by 254 nm UV-light with different duration. With increasing 254 nm UV-light exposure duration, both the intensities of the Bi^{3+} excitation D-band and A-band gradually decrease. This will be attributed to the valence state change from Bi^{3+} to Bi^{4+}. Fig. 3(g) gives the PL spectra (λ_{ex}=300 nm) of LiScGeO$_4$:0.003Bi^{3+} after being irradiated by 254 nm UV-light with a duration from 0 until 300 s in the dark. The ratios of the integrated PL intensity from 308 to 500 nm without 254 nm UV-light illumination to that with 254 nm UV-light illumination are listed as percentages in the legend in Fig. 3(g). The integrated PL intensity gradually decreases with increasing 254 nm UV-light exposure time, further evidencing the valence state change of Bi$^{3+} \rightarrow$Bi^{4+}. Fig. 3(h) shows the PL spectra (λ_{ex}=300 nm) of LiScGeO$_4$:0.003Bi^{3+} after being charged by 254 nm UV-light for 300 s and then illuminated by 365 nm UV-light with different duration from 0 until 240 s in the dark. The PL intensity can be recovered with 365 nm UV-light stimulation. This will be attributed to the valence state change of Bi$^{4+} \rightarrow$Bi^{3+} which is associated with electron liberation from traps upon 365 nm stimulation that recombines with Bi^{4+} to form Bi^{3+}.

Fig. 3(i) shows the photoluminescence decay curves (λ_{em}=360 nm) of LiScGeO$_4$:0.003Bi^{3+} upon 310 nm excitation after being charged by 254 nm UV-light with a duration from 0 until 600 s in the dark. The calculated decay time has been provided in the legend of Fig. 3(i). The average decay lifetime is about 4.4 μs. The charging by 254 nm illumination will reduce the Bi^{3+} concentration but not necessarily affect the Bi^{3+} decay time.

Fig. 3(j) shows a 2D contour plot of temperature dependent photoluminescence spectra from 10 to 310 K for LiScGeO$_4$:0.05Bi^{3+} upon the Bi^{3+} D-band (λ_{ex}=232.6 nm) excitation. Their integrated PL intensity as a function of temperature is shown in Fig. 3(k). It first decreases from 10 to ~150 K, then increases from ~150 to ~260 K, and finally decreases

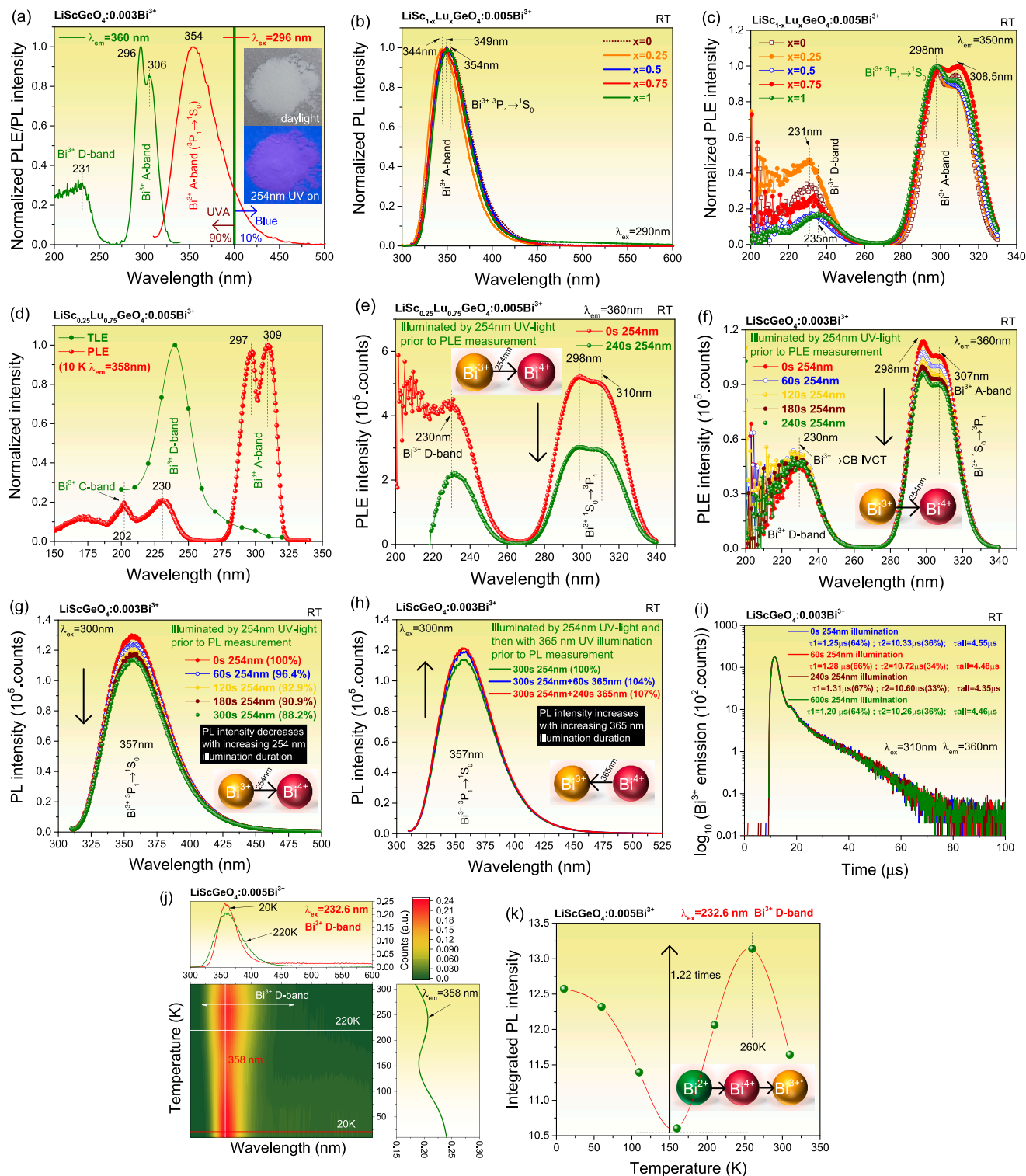**Fig. 3.** PLE and PL spectra for (a) LiScGeO$_4$:0.003Bi^{3+} and (b), (c) LiSc$_{1-x}$Lu$_x$GeO$_4$:0.005Bi^{3+}. (d) A comparison of photoluminescence excitation (PLE) spectrum (λ_{em}=358 nm) at 10 K and thermoluminescence excitation (TLE) spectrum for LiSc$_{0.25}$Lu$_{0.75}$GeO$_4$:0.005Bi^{3+}. (e) PLE spectra of LiSc$_{0.25}$Lu$_{0.75}$GeO$_4$:0.005Bi^{3+} after being illuminated by a Hg lamp. (f) PLE (λ_{em}=360 nm) and (g) PL spectra (λ_{ex}=300 nm) for LiScGeO$_4$:0.003Bi^{3+} after being illuminated by 254 nm UV-light with different duration. (h) PL spectra of LiScGeO$_4$:0.003Bi^{3+} after being illuminated first by 300 s 254 nm UV-light and then with 365 nm UV-light for different duration. (i) Decay curves of LiScGeO$_4$:0.003Bi^{3+} after being illuminated by 254 nm UV-light. (j) PL spectra (λ_{ex}=232.6 nm) and (k) integrated PL intensities as a function of temperature from 10 to 310 K for LiScGeO$_4$:0.005Bi^{3+}.

from ~260 to ~310 K. The PL increase between ~150 and 310 K will be attributed to the electron release from Bi^{2+} and recombination with the holes stored at Bi^{4+}, yielding enhancement of Bi^{3+} *A*-band emission.

3.2. Demonstrating Bi^{3+} as a deep hole trapping and recombination center for color-tailorable persistent luminescence

In Ref. [37], Bi^{3+}, Pr^{3+}, and Tb^{3+} all provide deep hole traps, but Bi^{3+} can also act as a 0.74±0.5 eV shallow electron trap based on the prediction of VRBE diagram in Fig. 1. In the discussion part, we will discuss the mechanism where an electron is released from Bi^{2+} to recombine with Bi^{4+}, Pr^{4+}, Tb^{4+}. To develop emission-tailorable phosphors with unique white and infrared afterglow for anti-counterfeiting application, Dy^{3+} and Cr^{3+} are co-doped with Bi^{3+} by exploiting energy transfer processes. Fig. 4(a) presents the RT isothermal decay spectra of $LiScGeO_4$:$0.003Bi^{3+}$ after being irradiated by 254 nm UV-light (~300 µW/cm²) for 60 s. More than 0.5 h Bi^{3+} $^3P_1 \rightarrow {}^1S_0$ (UVA) afterglow can be detected. The same applies to the $LiSc_{0.25}Lu_{0.75}GeO_4$:$0.005Bi^{3+}$

in Fig. S3. Fig. 4(b) until 4(d) give the RT isothermal decay spectra for $LiScGeO_4$:$0.005Bi^{3+}$, $0.005Tb^{3+}$, $LiScGeO_4$:$0.003Bi^{3+}$, $0.005Pr^{3+}$, and $LiScGeO_4$:$0.003Bi^{3+}$, $0.005Dy^{3+}$ after being charged by 254 nm UV-light for 60 s. Besides observing the Bi^{3+} *A*-band afterglow, Tb^{3+}, Pr^{3+}, or Dy^{3+} $4f \rightarrow 4f$ afterglow can be detected. The color coordinates of the afterglow spectra recorded at 5 s after 254 nm UV-light charging is provided in Fig. 4(i). Fig. 4(h) shows a RT isothermal decay spectrum for $LiScGeO_4$:$0.005Bi^{3+}$, $0.005Cr^{3+}$ after being illuminated by 254 nm UV-light for 240 s in the dark. The Cr^{3+} $^4T_2 \rightarrow {}^4A_2$ afterglow can be observed because of the energy transfer process from Bi^{3+} to Cr^{3+} as demonstrated in Fig. S23(b).

Since the Tb^{3+} $4f \rightarrow 4f$ afterglow covers the spectral range from 400 to 575 nm and the Pr^{3+} $4f \rightarrow 4f$ afterglow covers the spectral range from 590 to 700 nm, white afterglow may be realized through adjusting the concentration of Bi^{3+}, Tb^{3+}, or Pr^{3+}. Fig. 4(e) and 4(f) show the RT isothermal decay spectra of Bi^{3+}, Tb^{3+}, and Pr^{3+}-codoped $LiSc_{0.25}Lu_{0.75}GeO_4$ afterglow phosphors after being charged by 254 nm UV-light. More than 0.5 h white afterglow with a color coordinate of
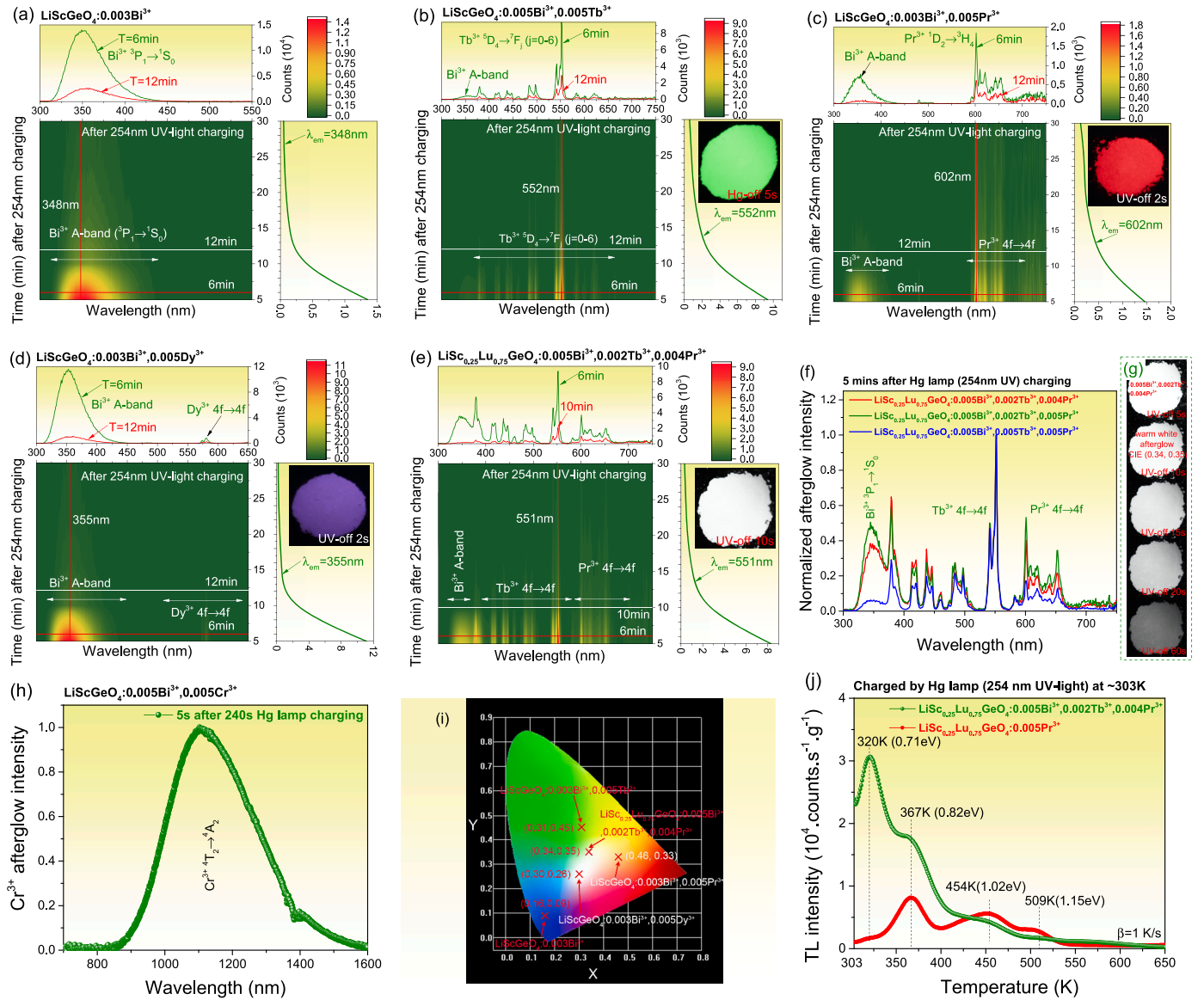

Fig. 4. (a) until (h) Room temperature (RT) isothermal afterglow spectra, (g) afterglow photographs, and (i) afterglow color coordinates for $LiScGeO_4$ and $LiSc_{0.25}Lu_{0.75}GeO_4$ doped with Bi^{3+}, Cr^{3+}, or different lanthanides after being illuminated by 254 nm UV-light in the dark. (j) TL glow curves of $LiSc_{0.25}Lu_{0.75}GeO_4$: $0.005Pr^{3+}$ and $LiSc_{0.25}Lu_{0.75}GeO_4$:$0.005Bi^{3+}$, $0.002Tb^{3+}$, $0.004Pr^{3+}$ after being irradiated by 254 nm UV-light for 20 s. The TL intensities have been corrected by the sample mass and the irradiation time. The emissions of Bi^{3+}, Tb^{3+}, and Pr^{3+} in the wavelength range from 300 to 750 nm was monitored during TL-readout.

(0.34, 0.35) can be measurable in LiSc$_{0.25}$Lu$_{0.75}$GeO$_4$: 0.005Bi^{3+}, 0.002Tb^{3+}, 0.004Pr^{3+}.

Fig. 4(j) compares the TL glow curves at β=1 K/s for LiSc$_{0.25}$Lu$_{0.75}$GeO$_4$:0.005Bi^{3+}, 0.002Tb^{3+}, 0.004Pr^{3+} and LiSc$_{0.25}$Lu$_{0.75}$GeO$_4$:0.005Pr^{3+} after being irradiated by 254 nm UV-light for 20 s. Stronger TL intensity at 320 K appears in LiSc$_{0.25}$Lu$_{0.75}$GeO$_4$:0.005Bi^{3+}, 0.002Tb^{3+}, 0.004Pr^{3+}.

3.3. Demonstrating Bi^{3+} as a shallow electron trapping center in LiSc$_{1-x}$Lu$_x$GeO$_4$

In the VRBE diagram in Fig. 1, Bi^{3+} is predicted to act as a 0.74±0.5 eV deep electron trapping center. To understand the role of Bi^{3+} during the charge carrier trapping process, a thermoluminescence study has been carried out for the Bi^{3+} doped LiSc$_{1-x}$Lu$_x$GeO$_4$ compounds.

Fig. 5(a) presents the above 100 K thermoluminescence emission (TLEM) spectra measured at β=1 K/s for LiScGeO$_4$:0.005Pr^{3+} after being irradiated by X-rays at 100 K. Two TL glow bands peaked at ~240 and

256 K with Pr^{3+} typical 4f→4f emissions in the spectral range from 550 to 950 nm are observed. They will be attributed to electron liberation from intrinsic defects in LiScGeO$_4$:0.005Pr^{3+} and recombination with the hole stored at Pr^{4+}. Fig. 5(b) shows the above 100 K TLEM spectra for X-ray charged LiScGeO$_4$:0.003Bi^{3+}. Different than that in LiScGeO$_4$:0.005Pr^{3+}, a new and strong TL glow band peaked near 268 K with Bi^{3+} typical $^3P_1→^1S_0$ (A-band) emission appears in LiScGeO$_4$:0.003Bi^{3+}. Herein, the TL band peaked about 268 K is named the Bi^{2+} TL band. It will be attributed to electron release from Bi^{2+} and recombination with the hole captured at Bi^{4+} to yield Bi^{3+} $^3P_1→^1S_0$ transition. Fig. 5(c) gives the above 100 K TLEM spectra for LiScGeO$_4$:0.003Bi^{3+}, 0.005Pr^{3+} after being irradiated by X-rays. Similar to that in LiScGeO$_4$:0.003Bi^{3+}, a weak Bi^{3+} *A*-band emission is observed in Fig. 5(c). The same TL glow band peaked near 268 K with the Pr^{3+} typical 4f→4f emissions are observed in LiScGeO$_4$:0.003Bi^{3+}, 0.005Pr^{3+}. It will be assigned to electron release from Bi^{2+} and recombination with the hole trapped at Pr^{4+} to generate the Pr^{3+} 4f→4f emissions.
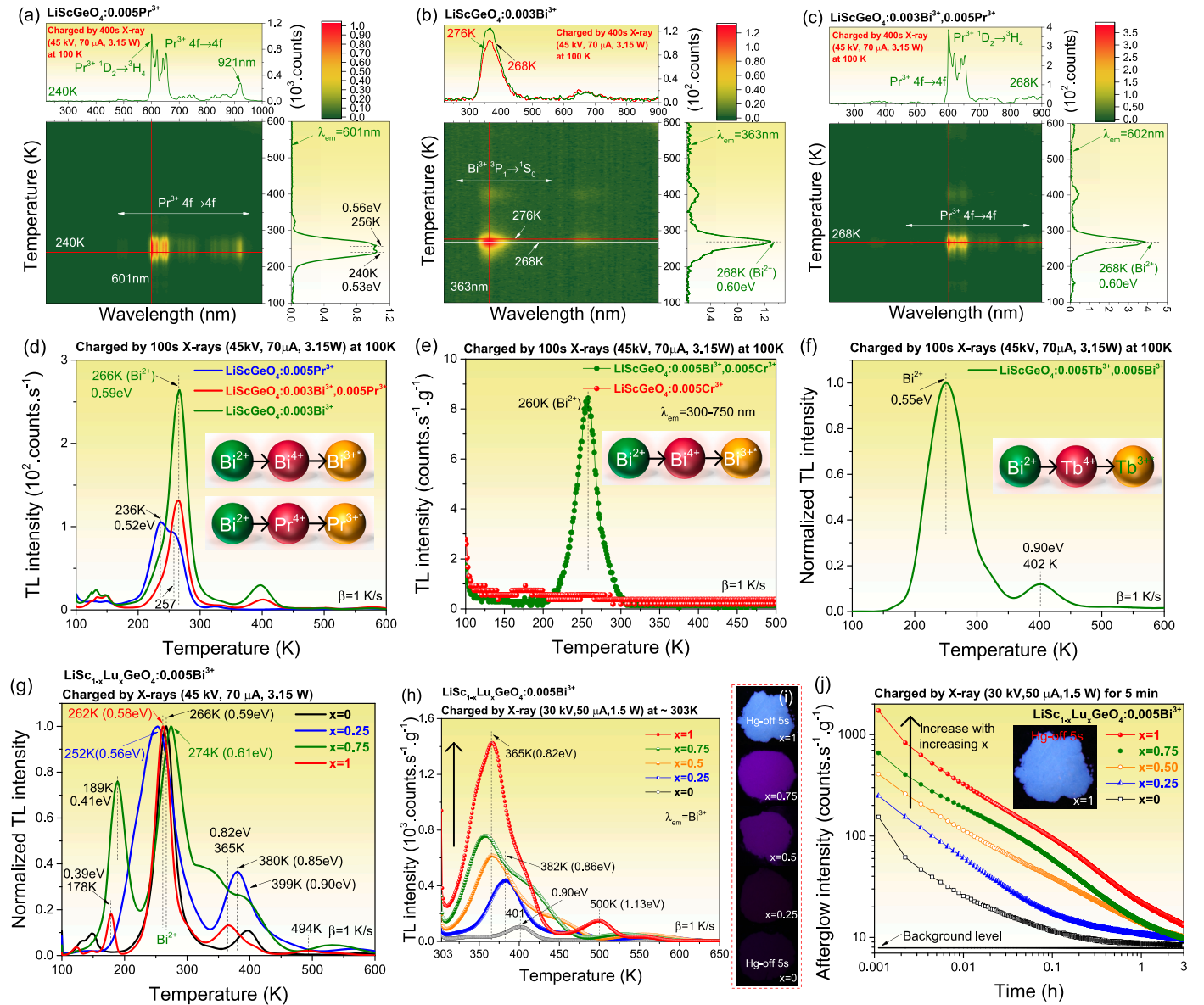

Fig. 5. (a) until (c) Above 100 K thermoluminescence emission (TLEM) spectra, (d) until (g) above 100 K, and (h) above 303 K TL glow curves of Bi^{3+}, Tb^{3+}, Pr^{3+}, or Cr^{3+} doped LiSc$_{1-x}$Lu$_x$GeO$_4$ (x = 0 until 1) after being irradiated by X-rays in the dark. (i) Afterglow photographs recorded at 5 s after 254 nm UV-light charging and (j) RT isothermal decay curves after being charged by 300 s X-rays for LiSc$_{1-x}$Lu$_x$GeO$_4$: 0.005Bi^{3+}. The afterglow intensities in (j) are corrected by the irradiation time and sample mass for a fair intensity comparison.

Fig. 5(d) until 5(f) compare the TL glow curves of Bi^{3+}, Cr^{3+}, or/and lanthanides doped $LiScGeO_4$ after being irradiated by X-rays at 100 K in the dark. A new and intense TL glow band peaked at about 260 K appears in Bi^{3+}-codoped $LiScGeO_4$, which is consistent with the TLEM spectra as shown in Fig. 5(a), (c). The TL mechanisms are illustrated in the legends of Fig. 5(d) until (f).

To further verify electron release from Bi^{2+}, Fig. 5(g) compares the above 100 K TL glow curves recorded at β=1 K/s for $LiSc_{1-x}Lu_xGeO_4$:0.005Bi^{3+} ($x = 0$ until 1) after being charged by X-rays at 100 K. With increasing x from 0 to 1, about 4 K shifting towards lower temperature appears in the Bi^{2+} TL glow band. Broadening of the Bi^{2+} TL glow band is observed for $x = 0.25$ and $x = 0.75$. Since the Bi^{2+} TL glow band emerges in the temperature range from 200 to 350 K, electron release from Bi^{2+} by thermal activation at RT will yield Bi^{3+} persistent luminescence.

Fig. 5(h) gives the above 303 K TL glow curves of $LiSc_{1-x}Lu_xGeO_4$:0.005Bi^{3+} after being illuminated by X-rays in the dark at RT. With increasing x from 0 to 1, TL glow band shifting from 401 to 365 K appears. The integrated TL intensity gradually increases with increasing x. It then leads to gradual enhancement of the RT isothermal afterglow intensity with increasing x. This is evidenced by the afterglow photographs in Fig. 5(i) and the decay curves in Fig. 5(j).

Fig. 5(j) presents the RT isothermal decay curves of $LiSc_{1-x}Lu_xGeO_4$:0.005Bi^{3+} ($x = 0$ until 1) after being illuminated by X-rays for 300 s in the dark. The Bi^{3+} afterglow intensity gradually increases with increasing x. Compared with the background level of the utilized photomultiplier, more than 3 h Bi^{3+} afterglow can be recordable for $x = 0$ to $x = 1$.
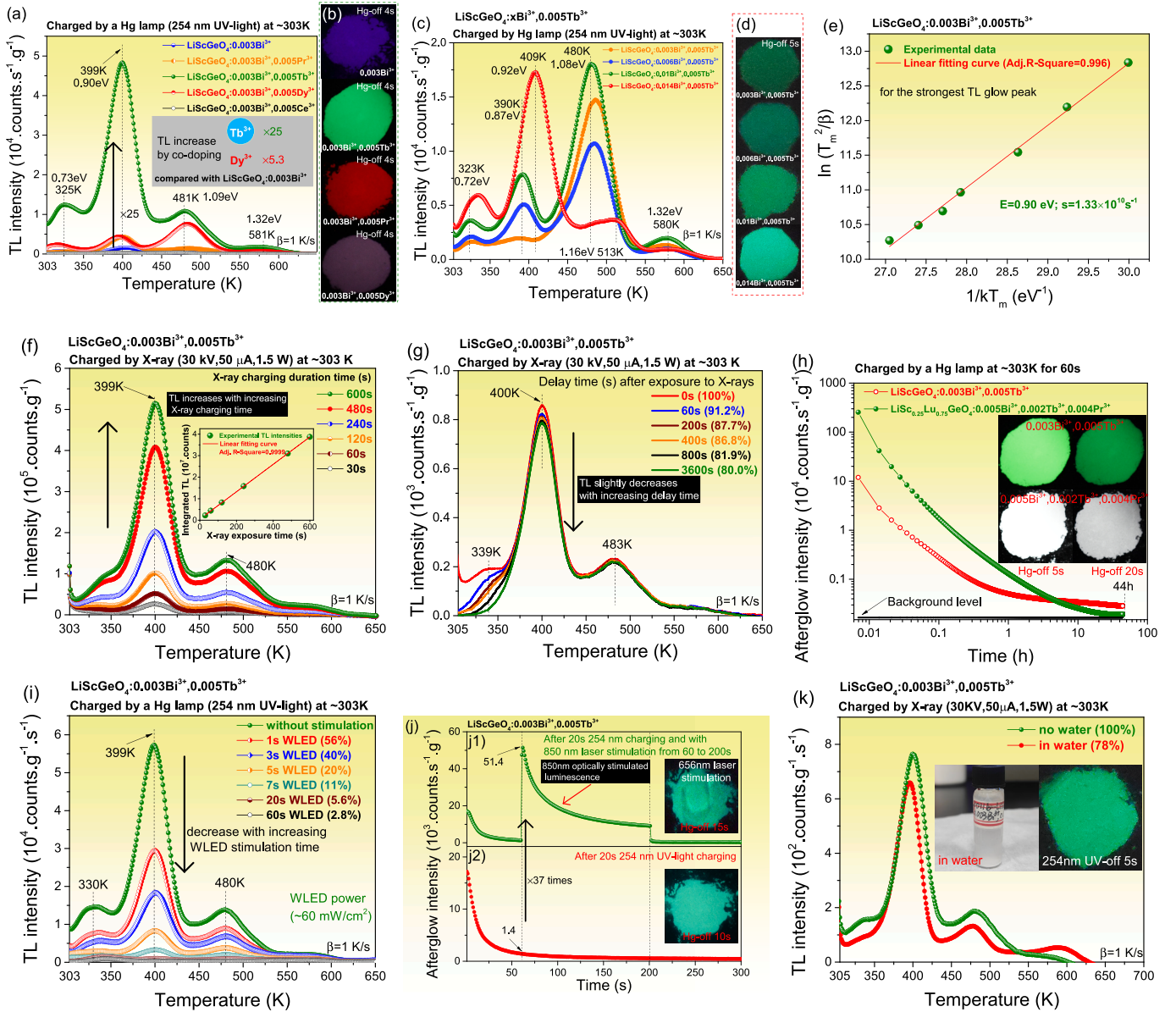
Fig. 6. TL glow curves recorded at β=1 K/s and afterglow photographs for (a), (b) $LiScGeO_4$:0.003Bi^{3+}, 0.005Ln^{3+} (Ln=Pr, Tb, or Dy) and (c), (d) $LiScGeO_4$:xBi^{3+}, 0.005Tb^{3+} after 254 nm UV-light charging. (e) A variable heating rate plot, (f) TL glow curves after being irradiated by X-rays with different duration, (g) TL fading characteristic, (h) RT isothermal decay curves, (i) TL glow curves after being first charged by 254 nm UV-light for 20 s and then illuminated by a commercial WLED with different duration, (j) RT isothermal decay curves after being first charged by 20 s 254 nm UV-light and then with 850 nm infrared light stimulation, and (k) TL glow curve for $LiScGeO_4$:0.003Bi^{3+}, 0.005Tb^{3+} after exposure to water.

3.4. Developing smart storage phosphors by using Bi^{3+} as a hole trapping and recombination center

Based on Bi^{3+} as a hole trapping and recombination center, a co-doping strategy has been explored for Bi^{3+} and Ln^{3+} (Ln=Tb, Pr, or Dy) doped $LiSc_{1-x}Lu_xGeO_4$ compounds to develop smart storage phosphors.

Fig. 6(a) shows the TL glow curves for $LiScGeO_4:0.003Bi^{3+}$ and $LiScGeO_4:0.003Bi^{3+}, 0.005Ln^{3+}$ (Ln=Pr, Tb, or Dy) after being irradiated by 254 nm UV-light for 20 s. TL glow bands peaked near 325, 399, and 481 K appear for all samples. They will be attributed to electron trapping defects. The Ln^{3+} co-doping not only leads to color tailorable afterglow in Fig. 6(b), but also results in stronger TL intensities in Fig. 6(a). Compared with the $LiScGeO_4:0.003Bi^{3+}$, the integrated TL intensity from 303 to 650 K has been increased by 25 times for $LiScGeO_4:0.003Bi^{3+}, 0.005Tb^{3+}$ and by about 5.3 times for $LiScGeO_4:0.003Bi^{3+}, 0.005Dy^{3+}$. Since $LiScGeO_4:0.003Bi^{3+}, 0.005Tb^{3+}$ has the strongest TL intensity, Bi^{3+}, Tb^{3+}-codoped $LiScGeO_4$ has been studied further.

Fig. 6(c) shows the TL glow curves for $LiScGeO_4:xBi^{3+}, 0.005Tb^{3+}$ (x = 0.003 until 0.014) after being charged by 254 nm UV-light for 20 s in the dark. With increasing x, the intensities of TL glow bands peaked near 323 and ~375 K gradually increase. Since these TL bands are close to

RT, stronger afterglow appears with increasing x. This is illustrated by the afterglow photographs as shown in Fig. 6(d).

Assuming that thermoluminescence is realized through a first-order recombination kinetics, one can estimate the electron trapping depths by utilizing a variable heating rate plot with the following equation [63–66]:

$$\ln\left(\frac{T_m^{\ 2}}{\beta}\right) = \frac{E}{kT_m} + \ln\left(\frac{E}{ks}\right) \tag{1}$$

where β means the used heating rate (K/s) which changes from β=0.4 K/s to β=6.4 K/s in Fig. S13, T_m is the experimentally observed temperature (K) of a TL glow peak at a given β, k means the Boltzmann constant, E is the trapping depth (eV), and s denotes the frequency factor for the studied compound.

Since $LiScGeO_4:0.003Bi^{3+}, 0.005Tb^{3+}$ has good charge carrier storage capacity, it has been further studied for developing smart storage phosphors. Fig. 6(e) provides the variable heating rate plot of $LiScGeO_4:0.003Bi^{3+}, 0.005Tb^{3+}$. For the TL glow peak at ~399 K in Fig. 6(a), a trapping depth of ~0.90 eV is determined from the slope of the fitted linear line through the data in Fig. 6(e). The frequency factor for $LiScGeO_4:0.003Bi^{3+}, 0.005Tb^{3+}$ has been deduced to be $s = 1.33 \times 10^{10}\ s$

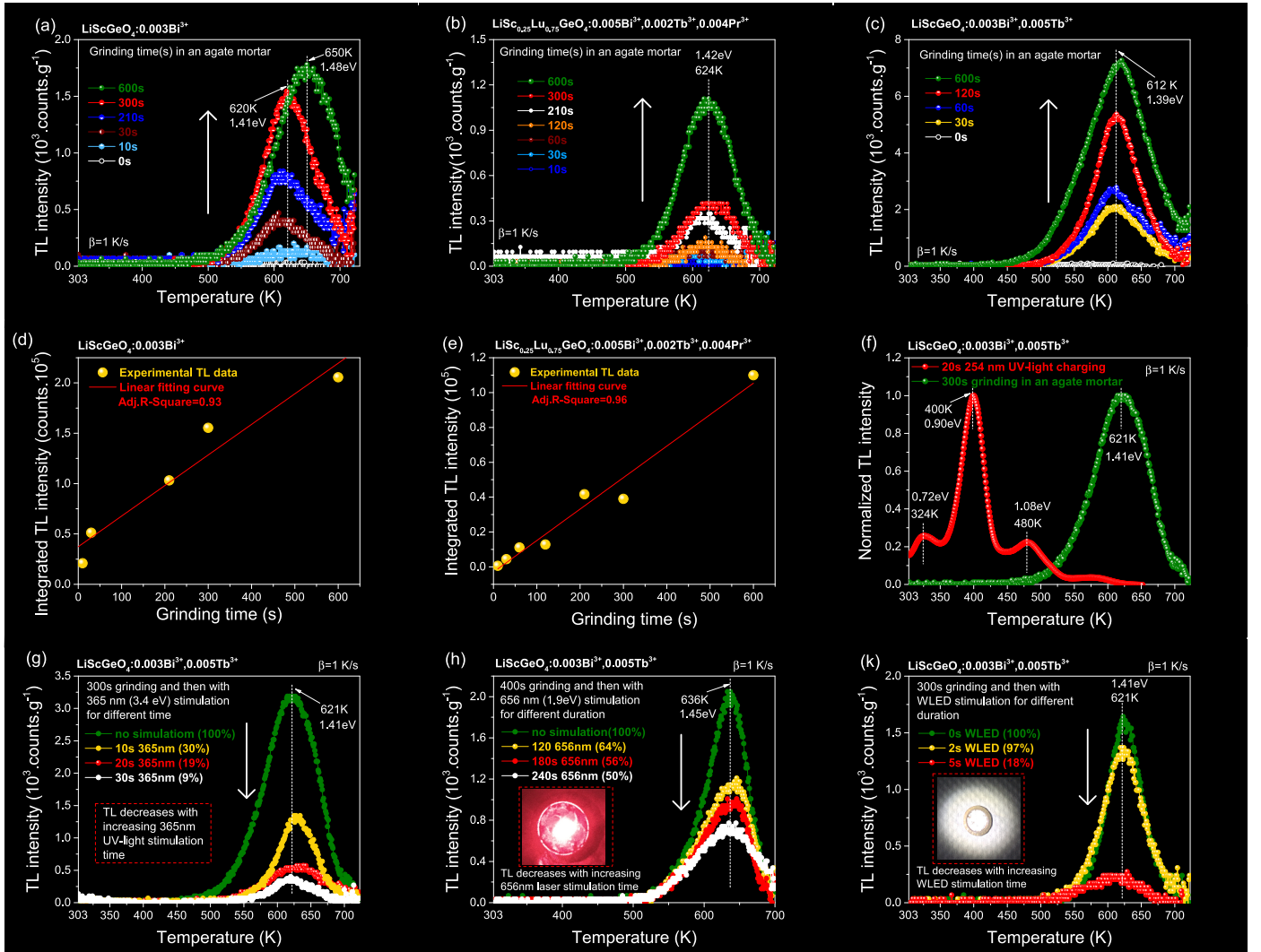**Fig. 7.** (a) until (f) TL glow curves and integrated TL intensities as a function of grinding time for $LiScGeO_4:0.003Bi^{3+}$, $LiSc_{0.25}Lu_{0.75}GeO_4:0.005Bi^{3+}, 0.002Tb^{3+}, 0.004Pr^{3+}$, and $LiScGeO_4:0.003Bi^{3+}, 0.005Tb^{3+}$ after being charged by grinding in an agate mortar with different time in the dark. TL glow curves measured at β=1 K/s for $LiScGeO_4:0.003Bi^{3+}, 0.005Tb^{3+}$ after first being charged by grinding and then illuminated by (g) 365 nm UV-light, (h) a 656 nm red laser beam, or (k) a WLED lamp with different duration in the dark.

$^{-1}$ from the intercept with the vertical axis. The trapping depths for different TL glow peaks like in Figs. 5, 6(a), (c), and 7 are then roughly estimated by applying Eq. (1) with β=1 K/s, $s = 1.33 \times 10^{10} s^{-1}$, and the experimentally observed T_m values.

Fig. 6(f) shows the TL glow curves recorded at β=1 K/s for LiScGeO$_4$:0.003Bi^{3+}, 0.005Tb^{3+} after being irradiated by X-rays with different duration from 30 s to 600 s in the dark. The integrated TL intensity from 303 to 650 K as a function of X-ray exposure duration has been provided in the inset of Fig. 6(f). The integrated TL intensity linearly increases with increasing X-ray exposure time. The same applies for LiScGeO$_4$:0.003Bi^{3+}, 0.005Dy^{3+} in Fig. S14. This indicates that they can act as potential X-ray dosimeters.

Fig. 6(g) presents the TL glow curves for LiScGeO$_4$:0.003Bi^{3+}, 0.005Tb^{3+} after being illuminated by X-rays for 200 s and then with different delay time from 0 until 1 h in the dark prior to TL-readout. With increasing the delay time, the intensity of the TL glow band peaked near 339 K rapidly decreases, while the intensity of the TL glow band peaked near 400 K slowly decreases. The TL glow band peaked near 483 K remains stationary. The ratios of the integrated TL intensity without delay to that of with different delay duration are given as percentages in the legend of Fig. 6(g). The TL intensity remains 80% after 1 h delay. The similar applies to LiScGeO$_4$:0.003Bi^{3+}, 0.005Dy^{3+} in Fig. S15.

Fig. 6(h) presents the room temperature isothermal decay curves of LiScGeO$_4$:0.003Bi^{3+}, 0.005Tb^{3+} and LiSc$_{0.25}$Lu$_{0.75}$GeO$_4$:0.005Bi^{3+}, 0.002Tb^{3+}, 0.004Pr^{3+} storage phosphors after being illuminated by 254 nm UV-light with a duration of 60 s in the dark. Compared with the background level of the used Hamamatsu R928P photomultiplier, more than 44 h green or white afterglow can be detectable in the dark.

Fig. 6(i) gives the TL glow curves for LiScGeO$_4$:0.003Bi^{3+}, 0.005Tb^{3+} after first being charged by 254 nm UV-light for 20 s and then illuminated by a commercial WLED lamp (~60 mW/cm^2) with different duration from 0 until 60 s in the dark. The intensities of the TL bands peaked near 330, 399, and 480 K gradually decrease with increasing WLED stimulation time. The similar applies for the stimulation light source of the 365 nm to 850 nm infrared light in other LiScGeO$_4$ family of compounds as shown in Fig. S17 and S18. The ratios of the integrated TL intensity with only 254 nm UV-light charging to that of with additional WLED illumination has been listed as percentages in the legend of Fig. 6(i). For 1 or 20 s WLED stimulation, about 44% or 94% stored charge carriers have been liberated.

Fig. 6(j) compares the RT isothermal decay curves of LiScGeO$_4$:0.003Bi^{3+}, 0.005Tb^{3+} after being charged by 20 s 254 nm UV-light or/and then illuminated by 850 nm infrared light from 60 to 200 s in the dark. Compared with no 850 nm stimulation in Fig. 6(j2), about 37 times stronger emission intensity emerges when the 850 nm infrared light is turned on in Fig. 6(j1). This is because of the electron liberation from traps by means of the 850 nm optically stimulated luminescence process. The phosphor area after being illuminated then has less intense afterglow. This physical feature with 656 nm laser stimulation has been used to smartly display an afterglow "U" letter as demonstrated in the inset of Fig. 6(j1).

The stability of a storage phosphor after being exposed to water is crucial for practical applications. Fig. 6(k) shows the TL glow curves of X-ray irradiated LiScGeO$_4$:0.003Bi^{3+}, 0.005Tb^{3+} without and with exposure to water for a duration of 1 h. The integrated TL intensity remains 78% after exposure to water for 1 h.

3.5. Evaluating potential non-real-time force sensing application with Bi^{3+} as a stable hole trap

Trapping of free charge carriers formed by mechanical stimulation has been explored in Bi^{3+} or/ and lanthanides doped LiScGeO$_4$ family of compounds for developing non-real-time force sensing application.

Fig. 7(a) until 7(c) provide the TL glow curves obtained at β=1 K/s for LiScGeO$_4$:0.003Bi^{3+}, LiSc$_{0.25}$Lu$_{0.75}$GeO$_4$:0.005Bi^{3+}, 0.002Tb^{3+}, 0.004Pr^{3+} solid solution, and LiScGeO$_4$:0.003Bi^{3+}, 0.005Tb^{3+} after

being charged by means of grinding in an agate mortar with different duration from 0 until 600 s in the dark. TL glow bands peaked near 610–650 K in the temperature range from 500 to 723 K are observed. The intensity of the TL glow band gradually increases with increasing the grinding time. The same applies to the LiScGeO$_4$:0.003Bi^{3+}, 0.005Pr^{3+} and LiScGeO$_4$:0.003Bi^{3+}, 0.005Dy^{3+} in Fig. S21. This means that trapping of free charge carriers formed by mechanical stimulation can be repeatedly observed in different LiScGeO$_4$ family of compounds.

Fig. 7(d) and 7(e) give the integrated TL intensities as a function of grinding duration for LiScGeO$_4$: 0.003Bi^{3+} and LiSc$_{0.25}$Lu$_{0.75}$GeO$_4$:0.005Bi^{3+}, 0.002Tb^{3+}, 0.004Pr^{3+} compounds. The integrated TL intensity linearly increases with increasing the grinding duration. This implies that the developed Bi^{3+} co-doped LiScGeO$_4$ family of compounds have potential utilization for non-real-time force sensing and storage application.

To unravel the trapping and release of free charge carriers formed by mechanical stimulation, LiScGeO$_4$: 0.003Bi^{3+}, 0.005Tb^{3+} has been studied further. Fig. 7(f) compares the TL glow curve measured at β=1 K/s for LiScGeO$_4$:0.003Bi^{3+}, 0.005Tb^{3+} after being charged by means of 254 nm UV-light illumination for 20 s or by grinding in an agate mortar with a pestle for 5 min in the dark. Different than by 254 nm UV-light charging, the TL glow band peaked at ~621 K is newly observed by mechanical grinding. Note that this new TL band can be repeatedly observed in LiScGeO$_4$:0.003Bi^{3+}, 0.005Tb^{3+} with mechanical grinding.

Fig. 7(g) until 7(k) show the TL glow curves at β=1 K/s for LiScGeO$_4$:0.003Bi^{3+}, 0.005Tb^{3+} after being charged by mechanical grinding and then followed by 365 nm, 656 nm laser, or a commercial WLED illumination for different duration in the dark. The ratios of the integrated TL intensity with only mechanical grinding to that of with additional optically illumination are listed as percentages in the legends of Fig. 7(g) until 7(k). The intensity of the TL glow band peaked at ~621 K gradually decreases with increasing the illumination duration.

3.6. Evaluating anti-counterfeiting and X-ray imaging applications with dual role of Bi^{3+} in trapping electrons and holes

Based on the dual role of Bi^{3+} in trapping electrons and holes, the developed LiScGeO$_4$ family of compounds have been further exploited for potential anti-counterfeiting and X-ray imaging applications.

A smart anti-counterfeiting application is first explored by utilizing multimode luminescence. Fig. 8(a) shows a text of "HQU". As illustrated in Fig. 8(b), it can be constituted of four special phosphors, i.e., the LiTaO$_3$:0.005Bi^{3+}, 0.002Dy^{3+} perovskite with photochromic and afterglow properties, Cs$_2$ZrCl$_6$:Sb^{3+} perovskite with high photoluminescence at both 254 and 365 nm excitation, LiScGeO$_4$:0.003Bi^{3+}, 0.015Tb^{3+} with green afterglow feature, and LiScGeO$_4$:0.003Bi^{3+}, 0.005Pr^{3+} with red afterglow property.

Fig. 8(c) and 8(d) show that the LiTaO$_3$:0.005Bi^{3+}, 0.002Dy^{3+} based letter "H" rapidly changes from white to brownish after being illuminated by 254 nm UV-light for 10 s. It can repeatedly change from brownish to white after being illuminated by 365 nm UV-light to 850 nm laser beam. The feature of the rapid and reversible photochromism can be used as one component for smart anti-counterfeiting application.

Fig. 8(e) and 8(f) demonstrate that the Cs$_2$ZrCl$_6$:Sb^{3+} perovskite based letter "Q" shows bright yellow emission upon both 254 nm and 365 nm excitation. The LiTaO$_3$:0.005Bi^{3+}, 0.002Dy^{3+} based letter "H", LiScGeO$_4$:0.003Bi^{3+}, 0.015Tb^{3+}, and LiScGeO$_4$:0.003Bi^{3+}, 0.005Pr^{3+} based "U" only show cyan, green, and red emissions upon 254 nm excitation in the dark. The tailorable photoluminescence color upon 254 or 365 nm excitation can be utilized as a feature for smart anti-counterfeiting application.

Fig. 8(g) and 8(h) show that color tailorable afterglow letter from cyan "H" to green and red "U" appears in the dark after being irradiated by 254 nm UV-light for 80 s. The afterglow is obtained because of the RT thermally stimulated Bi^{3+} A-band in LiTaO$_3$:0.005Bi^{3+}, 0.002Dy^{3+} and Tb^{3+} or Pr^{3+} 4f→4f emissions in LiScGeO$_4$:0.003Bi^{3+}, 0.015Tb^{3+} or
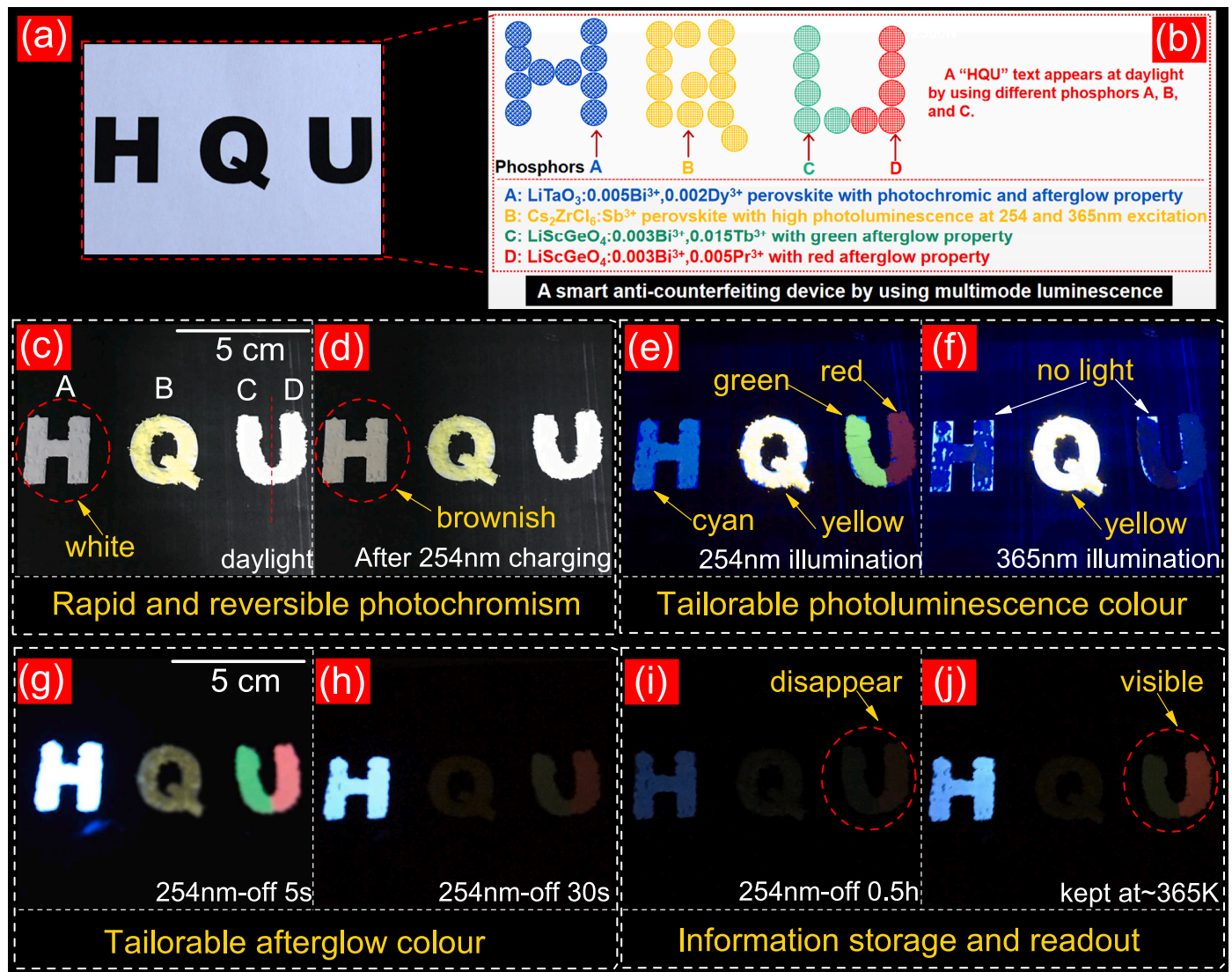
Fig. 8. (a) until (j) Proof-of-concept smart anti-counterfeiting application by using multimode luminescence from different phosphors with unique optical features, i. e., LiTaO$_3$:0.005Bi^{3+}, 0.002Dy^{3+}, Cs$_2$ZrCl$_6$:Sb^{3+}, LiScGeO$_4$:0.003Bi^{3+}, 0.015Tb^{3+}, and LiScGeO$_4$:0.003Bi^{3+}, 0.005Pr^{3+}.

LiScGeO$_4$:0.003Bi^{3+}, 0.005Pr^{3+}.

Fig. 8(i) shows that afterglow "H" and "U" gradually disappear in the dark with increasing fading time after 254 nm UV-light charging. 8(j) demonstrates that the colourful information storage and readout of letters "H" and "U" is realized by thermally stimulated Bi^{3+} *A*-band in LiTaO$_3$:0.005Bi^{3+}, 0.002Dy^{3+} and Tb^{3+} or Pr^{3+} 4f→4f emissions in LiScGeO$_4$:0.003Bi^{3+}, 0.015Tb^{3+} or LiScGeO$_4$:0.003Bi^{3+}, 0.005Pr^{3+} at 365 K. Note that the Bi^{3+} *A*-band afterglow in Bi^{3+}, Tb^{3+}- or Bi^{3+}, Pr^{3+}-codoped LiScGeO$_4$ is not visible to the eye, but can be detected by using a photomultiplier or a QE65000 spectrometer.

To develop more advanced anti-counterfeiting application, ultraviolet-A (UVA), color-tailorable, and white afterglow has further been explored.

Fig. 9(a) shows how an afterglow phosphor can be used for QR code based information storage and anti-counterfeiting applications. Afterglow phosphors LiScGeO$_4$:0.005Bi^{3+}, 0.005Tb^{3+}, LiSc$_{0.25}$Lu$_{0.75}$GeO$_4$:0.005Tb^{3+}, LiSc$_{0.25}$Lu$_{0.75}$GeO$_4$:0.005Pr^{3+}, or LiSc$_{0.25}$Lu$_{0.75}$GeO$_4$:0.005Bi^{3+}, 0.002Tb^{3+}, 0.004Pr^{3+} have been respectively dispersed in transparent ink solution to print different QR codes on a sheet of a normal paper with a screen printing technique as shown in Fig. 9(b1), 9 (c1), 9(d1), and 9(e1). These QR codes are almost invisible to an eye during daylight. This concealment characteristic can be used as a feature

for advanced anti-counterfeiting application. After 254 nm UV-light illumination, green in Fig. 9(b2), cyan in Fig. 9(c2), red in Fig. 9(d2), and white in Fig. 9(e2) until 9(e4) afterglow QR codes are visible in the dark. The afterglow intensities are strong enough to be scanned by a mobile phone to read out the hidden information in the dark as shown in Fig. 9(b3), 9(c3), 9(d3), and 9(e5).

The white afterglow QR code in Fig. 9(e2) until 9(e4) is unique, which is rarely reported. It can be correctly visible to an eye in the dark compared with other color afterglow QR codes in Fig. 9(b2), 9(c2), and 9 (d2). Another unique feature for the white afterglow QR code in Fig. 9 (e2) is that it shows special ultraviolet-A (UVA) Bi^{3+} $^3P_1 \rightarrow ^1S_0$ persistent luminescence in the spectral range from 300 to 400 nm. The UVA afterglow can only be detected by a spectrometer, which can be utilized as a secret feature for anti-counterfeiting application. Note that LiScGeO$_4$:0.005Bi^{3+}, 0.005Cr^{3+} with unique Cr^{3+} infrared afterglow can be potentially used for developing anti-counterfeiting QR code.

Bi^{3+} as a shallow electron trap has been exploited for developing smart labeling. Fig. 10(a) presents the above 100 K TL glow curve measured at β=1 K/s for LiSc$_{0.25}$Lu$_{0.75}$GeO$_4$:0.005Bi^{3+}, 0.002Tb^{3+}, 0.004Pr^{3+} after being irradiated by X-rays for 100 s at 100 K. A Bi^{2+} TL glow band peaked at near 270 K emerges in the temperature range from ~200 to 350 K. LiSc$_{0.25}$Lu$_{0.75}$GeO$_4$:0.005Bi^{3+}, 0.002Tb^{3+}, 0.004Pr^{3+}
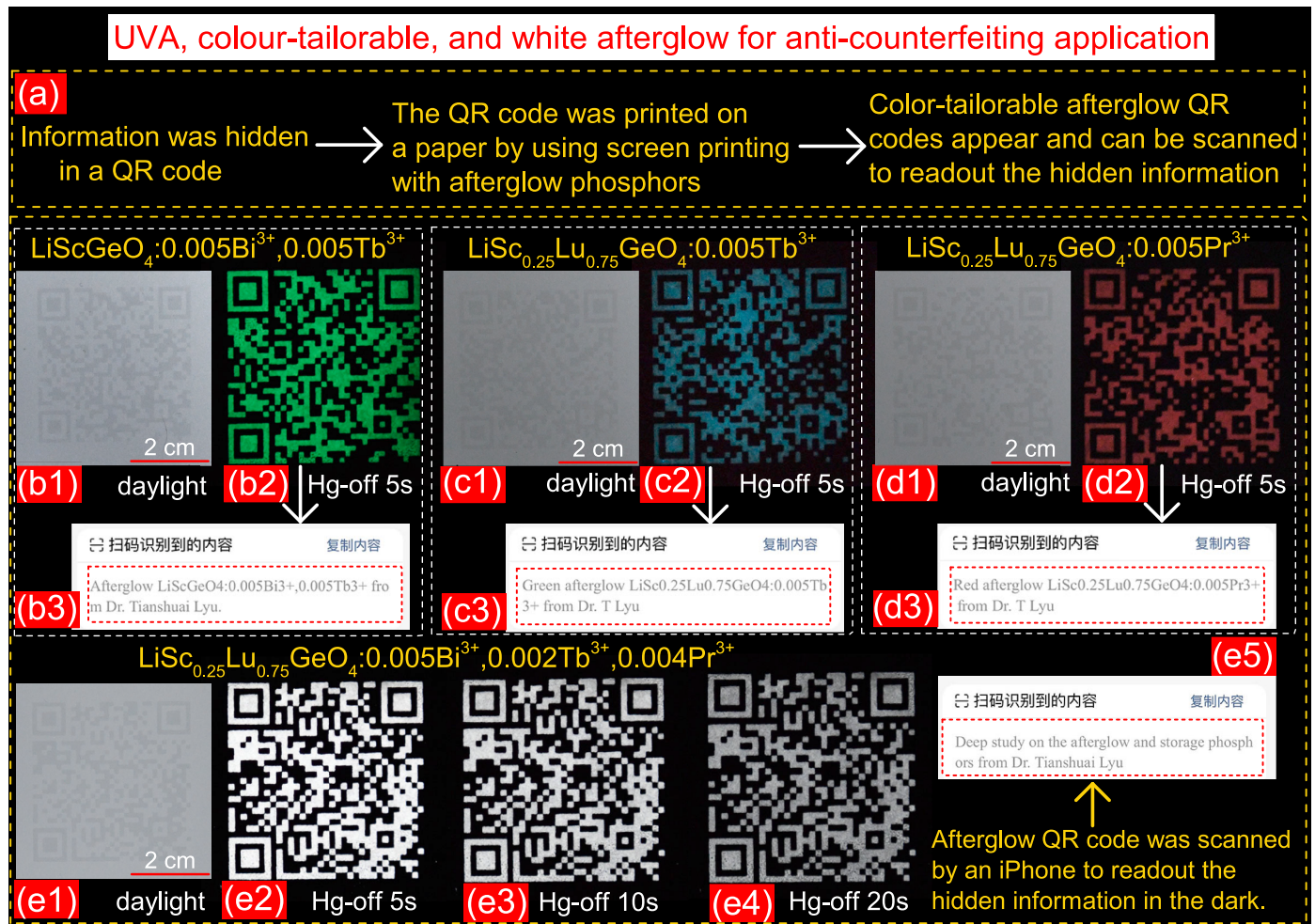
Fig. 9. (a) until (e) Proof-of-concept QR code anti-counterfeiting application by using color-tailorable and white afterglow from the developed LiScGeO$_4$ and LiSc$_{0.25}$Lu$_{0.75}$GeO$_4$ doped with Bi^{3+}, Tb^{3+}, or Pr^{3+} after being irradiated by 254 nm UV-light in the dark.

has been dispersed in silicone gel to make a flexible film. Fig. 10(b) illustrates that it can be placed on the surface of a bottle to monitor the storage and transport of vaccines that should be kept at low temperature like 200 K. During exposure to X-ray or 254 nm UV-light in Fig. 10(c) and 10(e), the phosphor in the film is charged. A smart label can be flexibly designed after first being charged by 254 nm UV-light and then selectively illuminated by 656 nm laser as shown in Fig. 10(g). If the ambient temperature has been increased from 200 K to RT (~300 K), white afterglow labels are clearly visible to the eye in the dark like in Fig. 10(d), 10(f), and 10(h). If the ambient temperature is always kept at 200 K, one should observe the Bi^{2+} TL band peaked at 270 K as shown in Fig. 10(a).

The developed LiScGeO$_4$:0.003Bi^{3+}, 0.005Tb^{3+} was first sifted by a 200 mesh screen and then dispersed in silicone gel to fabricate a flexible X-ray imaging film as shown in Fig. 11(a). A bright green afterglow film appears in Fig. 11(b) and 11(c) in the dark because of room temperature thermally stimulated Tb^{3+} 4f→4f emissions from LiScGeO$_4$:0.003Bi^{3+}, 0.005Tb^{3+} after being charged by 254 nm UV-light.

Fig. 11(d) illustrates that the LiScGeO$_4$:0.003Bi^{3+}, 0.005Tb^{3+} based film is placed underneath a black object. They are perpendicularly exposed to X-rays in the dark. After X-ray exposure, the black object has been removed from the film. An X-ray imaging photograph of a chip is visible to the eye in the dark because of thermally stimulated Tb^{3+} 4f→4f emissions at RT in Fig. 11(e) or 380 K in Fig. 11(f).

The LiSc$_{0.25}$Lu$_{0.75}$GeO$_4$:0.005Bi^{3+}, 0.002Tb^{3+}, 0.004Pr^{3+} based flexible film has also been explored for X-ray imaging. Fig. 11(g1) until

11(g3) present that the film was placed underneath a red pen, chicken claws, and a Pb based X-ray imaging plate. They are perpendicularly exposed to X-rays in the dark. After X-ray exposure, the red pen, chicken claws, and Pb based plate were removed. The film was kept at about 403 K to get the nice X-ray imaging photographs as shown in Fig. 11(g4) until 11(g6). One then can distinguish the inner structure of the red pen in Fig. 11(g4), the hard bones, and tissues of the chicken claws in Fig. 11 (g5). The X-ray imaging resolution is roughly determined to be ~20 lp/mm in Fig. 11(g6). Compared with the white color in Fig. 10(d), pink color appears in Fig. 11(g4) until 11(g6), possibly due to the decreased ratio of Tb^{3+} emissions to that of Pr^{3+} at ~403 K. This feature can be used as a secret component for developing temperature dependent anti-counterfeiting applications.

4. Discussion

4.1. VRBE in the Bi^{2+} $^2P_{1/2}$ in LiScGeO$_4$ and LiLuGeO$_4$

Doping of bismuth into inorganic compounds is an interesting strategy to develop new optical storage and mechanoluminescence materials, for instance in Sr$_3$Y$_2$Ge$_3$O$_{12}$:Bi^{3+} [67], SrZnSO:Bi^{3+} [68], MgGa$_2$O$_4$:Bi^{3+} [69], Ca$_{1-x}$Ba$_x$ZnOS:Bi^{3+} [48], and SrBaZn$_2$Ga$_2$O$_7$:Bi^{3+} [61,62]. However, bismuth has different valence states like Bi^{2+}, Bi^{3+}, and Bi^{4+}. The understanding of the luminescence mechanism, trapping, and de-trapping of electrons and holes in Bi^{2+} and Bi^{3+} doped compounds always remains a challenge. We propose that a deeper
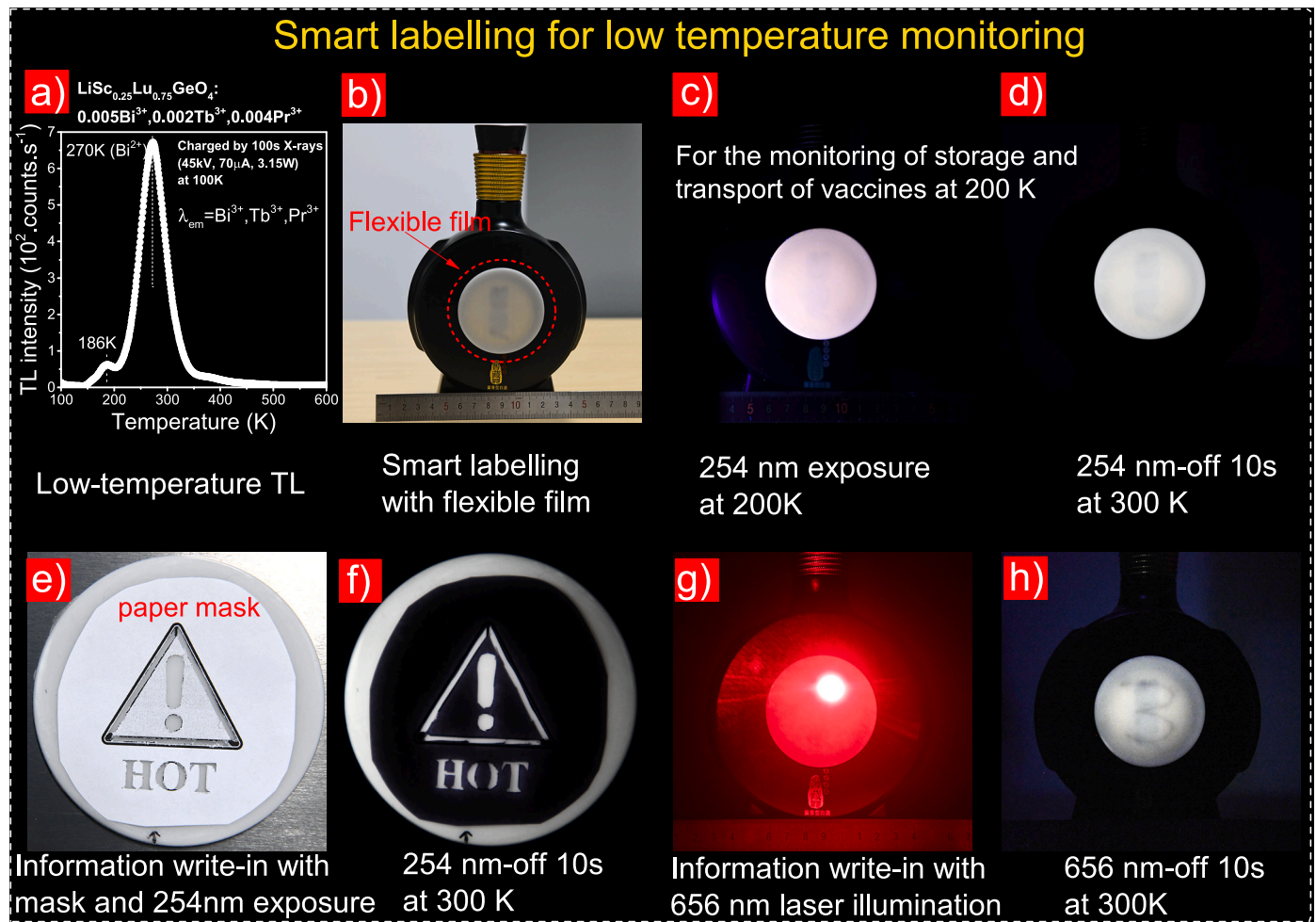
Fig. 10. (a) until (h) Proof-of-concept smart labeling for low temperature monitoring by using LiSc$_{0.25}$Lu$_{0.75}$GeO$_4$:0.005Bi^{3+}, 0.002Tb^{3+}, 0.004Pr^{3+} based silicone gel film.

understanding can be reached by obtaining the knowledge of the energy level locations of Bi^{3+} and Bi^{2+} in compounds. In a recent case study in Ref. [37], the photoluminescence excitation and emission spectra of Bi^{3+} single doped LiScGeO$_4$ were studied at 10 K. The results were used to determine the vacuum referred binding energies (VRBE) in the $^1S_0$, $^3P_1$, and $^1P_1$ states of Bi^{3+} in LiScGeO$_4$ as given in the VRBE diagram in Fig. 1. In Ref. [49], first principles calculations were performed on the Bi$^{3+/4+}$ and Bi$^{2+/3+}$ charge transition levels in LiScGeO$_4$. The calculated Bi^{3+} and Bi^{2+} ground states are 2.44 and 6.15 eV above the VB-top, respectively. It translates that the computed Bi^{3+} level is 1 eV higher than that in the VRBE diagram but the Bi^{2+} level is almost the same as that in our VRBE diagram in Fig. 1. However, the VRBE in the Bi^{2+} $^2P_{1/2}$ ground state in LiScGeO$_4$ has not been experimentally determined yet. The valence state change between Bi^{2+}, Bi^{3+}, and Bi^{4+} is still unclear.

In Ref. [70], spectroscopic data for Bi^{2+}-doped in 15 different inorganic compounds were compiled and analyzed. The VRBE in the Bi^{2+} $^2P_{1/2}$ ground state was found to be in the energy range from about −3 to −4 eV. Based on this result, the VRBE in the Bi^{2+} $^2P_{1/2}$ is first predicted to be about −3.5 ± 0.5 eV for LiScGeO$_4$ in Fig. 1. The same applies for LiLuGeO$_4$. It translates that Bi^{2+} may act as a ~0.74±0.5 eV deep electron trapping center in LiScGeO$_4$ and LiLuGeO$_4$.

Fig. 1 predicts that Bi^{3+} may work as a ~0.74±0.5 eV deep electron trap, while Tb^{3+}, Pr^{3+}, and Bi^{3+} work as about 2.19, 2.15, and 1.5 eV deep hole traps in LiScGeO$_4$. By combining Bi^{3+} with Tb^{3+}, Pr^{3+}, or Bi^{3+} itself, electron liberation from Bi^{2+} may lead to thermally stimulated Tb^{3+}, Pr^{3+}, or Bi^{3+} typical emissions but with a common TL glow peak during TL-readout. Indeed, this prediction is evidenced by the TLEM

spectra and TL glow curves as shown in Fig. 5(a) until 5(g) where a new and common TL glow band peaked at about 266 K emerges in the temperature range from 200 to ~320 K in Bi^{3+} co-doped LiScGeO$_4$. A similar TL band peaked at ~262 K also appears in LiLuGeO$_4$:0.005Bi^{3+} in Fig. 5(g). For LiSc$_{1-x}$Lu$_x$GeO$_4$:0.005Bi^{3+} (x = 0.25 or 0.75) solid solutions in Fig. 5(g), broadening of TL glow bands peaked at ~252 and 274 K is observed. It is related to a trap depth distribution feature in the solid solutions. It means that the VRBE at the CB bottom has site-to-site fluctuations which are based on the statistics in substituting *Sc* by Lu in LiSc$_{1-x}$Lu$_x$GeO$_4$:0.005Bi^{3+} (x = 0.25 or 0.75) solid solutions [66,71,72]. We therefore assign the TL glow band peaked at ~266 K to the electron liberation from Bi^{2+} to recombine with the holes stored at Bi^{4+}, Tb^{4+}, or Pr^{4+} to generate Bi^{3+} $^3P_1 \rightarrow {}^1S_0$, Tb^{3+}, or Pr^{3+} typical 4f→4f emissions. By using Eq. (1) with β=1 K/s, s = 1.33 × 10^{10} s^{-1}, and the experimentally observed T$_m$=266 or 262 K, the Bi^{2+} electron trapping depth has been roughly determined to be ~0.59 eV. The VRBE in the Bi^{2+} $^2P_{1/2}$ ground state is then deduced to be about −3.35 eV by subtracting 0.59 eV from the VRBE in the CB bottom of LiScGeO$_4$ or LiLuGeO$_4$. The obtained VRBE in the Bi^{2+} $^2P_{1/2}$ at −3.35 eV is consistent with the predicted value of −3.5 ± 0.5 eV.

4.2. Bi^{3+} negative quenching luminescence with valence state change of Bi^{2+}, Bi^{3+}, and Bi^{4+}

Fig. 3(k) shows the Bi^{3+} thermal quenching curve for LiScGeO$_4$:0.005Bi^{3+} from 10 to 310 K upon Bi^{3+} D-band excitation. A Bi^{3+} negative quenching luminescence phenomenon unexpectedly
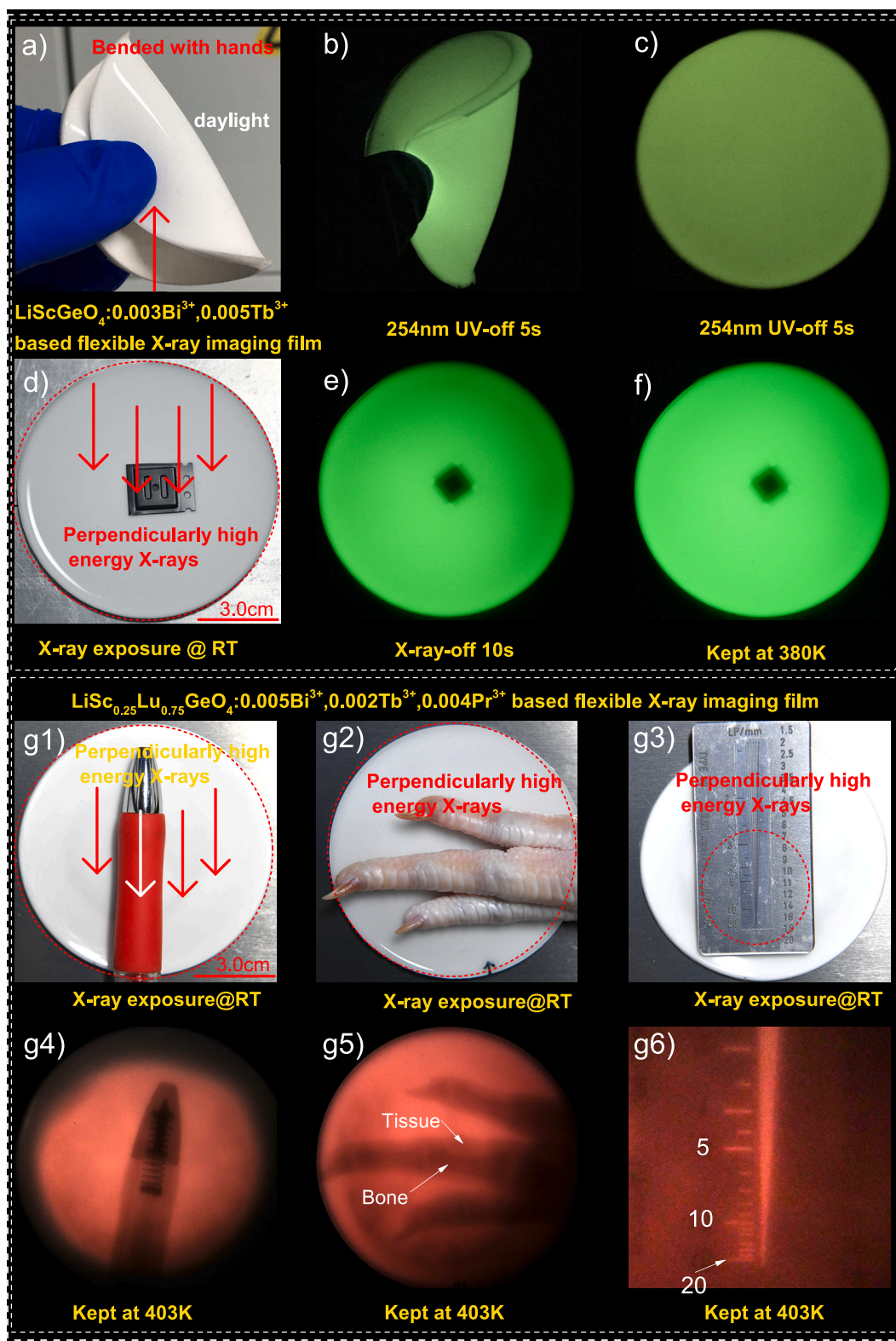
Fig. 11. (a) until (c) and (g1) The synthesized LiScGeO$_4$:0.003Bi^{3+}, 0.005Tb^{3+} and LiSc$_{0.25}$Lu$_{0.75}$GeO$_4$: 0.005Bi^{3+}, 0.002Tb^{3+}, 0.004Pr^{3+} storage phosphors have been dispersed into silicone gel to make storage phosphors based flexible X-ray imaging films. (d) until (f) and (g1) until (g6) Proof-of-concept X-ray imaging by using the developed flexible X-ray imaging films.

appears from 150 to 310 K. Compared with that at 160 K, 1.22 times stronger Bi^{3+} $^3P_1 \rightarrow {}^1S_0$ emission is observed at 260 K. Surprisingly, the Bi^{3+} negative quenching luminescence curve from 150 to 310 K in Fig. 3 (k) highly resembles the Bi^{2+} TL glow band peaked at ~266 K as shown in Fig. 5(b) until 5(g). Considering the thermoluminescence excitation (TLE) curve in Fig. 3(d), a model of trapping and de-trapping of electrons at Bi^{2+} is proposed to explain this special Bi^{3+} negative quenching luminescence phenomenon.

As illustrated in the VRBE diagram in Fig. 1, during 254 nm UV-light exposure, i.e., the Bi^{3+} D-band excitation, electron is excited from the Bi^{3+} $^1S_0$ ground state to the conduction band (CB), leading to the valence state change from Bi^{3+} to Bi^{4+}. The free electron can finally lead to generate normal Bi^{3+} A-band emission. It can also be captured by Bi^{3+} trap to form Bi^{2+} at 10 K. With increasing temperature from 10 to 150 K, the probability of the electron escape from the Bi^{3+} D-band to the CB increases. This leads to that Bi^{3+} A-band emission gradually decreases in Fig. 3(k) and Bi^{3+} trap filling occurs. Due to the trap filling, the concentration of Bi^{2+} and Bi^{4+} increases with increasing temperature. At 150 K, concentration of Bi^{2+} is so high and thermal release of the electron from Bi^{2+} rapidly occurs. When the temperature is above 150 K, the thermal activation energy gradually becomes high enough to liberate the electrons stored at Bi^{2+}. Recombination of electrons liberated from Bi^{2+} with the holes captured at Bi^{4+} releases energy that excites Bi^{3+} to its $^3P_1$ excited state. The Bi^{3+} $^3P_1 \rightarrow {}^1S_0$ emission then compensates the drop of the Bi^{3+} emission intensity by a conventional thermal quenching process with increasing temperature [73–75].

Fig. 3(e) until 3(g) show the PLE and PL spectra of $LiSc_{0.25}Lu_{0.75}GeO_4{:}0.005Bi^{3+}$ and $LiScGeO_4{:}0.003Bi^{3+}$ after being charged by 254 nm UV-light in the dark with different duration at RT. In Fig. 5(b), the Bi^{2+} TL glow band is below RT. It means that during Bi^{3+} D-band excitation, the free electrons can be captured at Bi^{2+} but rapidly and automatically be released by thermal stimulation at RT. The free electrons can be directly stored at unintended electron traps instead of at Bi^{2+}. The Bi^{3+} concentration is decreased by means of the valence change of $Bi^{3+} \rightarrow Bi^{4+}$. As evidenced by the PLE and PL spectra in Fig. 3 (e) until 3(g), the intensities of both the Bi^{3+} excitation and emission bands are dynamically decreased. Fig. 3(h) shows the PL spectra of $LiScGeO_4{:}0.003Bi^{3+}$ after first being charged by 254 nm UV-light for 300 s and then illuminated by 365 nm UV-light for different duration. The electron trapping depths for the above RT TL glow bands in $LiScGeO_4$ family of compounds are estimated to be in the range from ~0.7 to 1.3 eV in Figs. 5(h), 6(c), and S9. The energy of the 365 nm stimulation light (3.4 eV) is much higher than that of the electron trap depths (~0.7 to 1.3 eV). During 365 nm UV-light stimulation, a part of electrons stored at unintended electron trapping defects can be excited to conduction band, which can be partly captured by Bi^{4+} to form Bi^{3+}. This is consistent with the recovery of the Bi^{3+} A-band emission in Fig. 3(h).

4.3. Fully controlling trapping and de-trapping of charge carriers by thermal, optical, and mechanical stimulation

Fig. 5(g) and (h) compare the above 100 K and the above 303 K TL glow curves at $\beta=1$ K/s for $LiSc_{1-x}Lu_xGeO_4{:}0.005Bi^{3+}$ ($x = 0$ until 1) after X-ray charging. The TL glow bands peaked near 252–274 K in Fig. 5 (g) has been attributed to the electron liberation from Bi^{2+}. Figs. 1, 4(a), and 5(b) evidence that Bi^{3+} acts a ~1.6 eV deep hole trapping and recombination center in $LiScGeO_4$. The TL glow bands peaked in the range from near 365 K (0.82 eV) to 500 K (1.13 eV) are therefore related to unintended electron trapping defects in $LiSc_{1-x}Lu_xGeO_4{:}0.005Bi^{3+}$. The same applies to $LiScGeO_4{:}0.003Bi^{3+}$, $0.005Ln^{3+}$ in Fig. 6(a) and $LiScGeO_4{:}xBi^{3+}$, $0.005Tb^{3+}$ compounds in Fig. 6(c).

Fig. 6(g) shows the TL fading curves of $LiScGeO_4{:}0.003Bi^{3+}$, $0.005Tb^{3+}$ after being irradiated by X-rays. Gradual fading of TL bands peaked at 339 and 400 K emerges. During thermal stimulation at RT, electrons stored at unintended defects are released to recombine with the holes captured at Bi^{4+} or Tb^{4+}, producing Bi^{3+} $^3P_1 \rightarrow {}^1S_0$ or Tb^{3+} $^5D_4 \rightarrow {}^7F_j$ ($j = 0$–6) afterglow emissions as evidenced in Figs. 4(b) and 6 (h).

The TL curves in Figs. 6, S17, and S18 show that de-trapping of electrons from traps can be realized in the $LiScGeO_4$ family of compounds by stimulation with wide range of 365 nm to 850 nm infrared light. The energy of 365 nm (3.4 eV) to 850 nm (1.5 eV) is higher than that of the electron trapping depths from ~0.7 to 1.3 eV. Note that the energy is also higher than the hole trapping depths of Bi^{3+}, Pr^{3+}, and

Tb^{3+}. In principle these holes can also be excited to the VB. However, electrons in the CB will migrate much more rapidly than holes in the VB, and that recombination route is then expected to be dominant. During 365 nm to 850 nm stimulation, electrons are released from unintended electron capturing defects to the conduction band. Energy is released when they recombine with the holes stored at Bi^{4+}, Tb^{4+}, or Pr^{4+}. The released energy excites Bi^{3+}, Tb^{3+}, or Pr^{3+} to their excited states, then forming Bi^{3+} $^3P_1 \rightarrow {}^1S_0$, Tb^{3+}, or Pr^{3+} 4f→4f transitions [23,76].

The TL bands peaked at 610–650 K in Fig. 7(a) until (c) and S21 evidence that trapping and storage of charge carriers is realized in Bi^{3+} or/and Ln^{3+} (Ln=Tb, Pr, or Dy) doped $LiScGeO_4$ family of compounds with mechanical grinding. Compared with by 254 nm UV-light charging, these TL bands peaked at ~621 K are observed only when by grinding charging as demonstrated in Fig. 7(f). It means that new traps are formed by mechanical grinding. Their trapping depths are calculated to be ~1.41 to 1.48 eV by using Eq. (1) with $\beta=1$ K/s, $s = 1.33 \times 10^{10}$ s^{-1}, and T_m values. Based on the calculated trap depths, the vacuum referred binding energies in the energy levels for these traps are determined to be between about -4.17 and -4.24 eV. They are collectively denoted as force induced charge carrier storage (FICS) traps in Fig. 1. When the $LiScGeO_4$ family of compounds are excited by grinding in the dark, free electrons and holes are formed possibly by means of a triboelectricity [11,77–79] or piezoelectricity [80–83] related stimulation approach. The created electrons migrate freely in the conduction band and then are stored the traps FICS. The created holes are migrate freely through the valence band and then are eventually captured by Bi^{3+}, Tb^{3+}, or Pr^{3+}, creating Bi^{4+}, Tb^{4+}, or Pr^{4+}. Fig. 7(g) until (k) present the TL glow curves of $LiScGeO_4{:}0.003Bi^{3+}$, $0.005Tb^{3+}$ after being charged by grinding and then stimulated by 365 nm UV-light to 656 nm infrared laser. The determined electron trapping depth (~1.4 eV) for FICS traps is lower than the energies of 365 nm (3.4 eV) to 850 nm (1. 9 eV). During exposure to 365 nm to 656 nm laser, electrons are therefore liberated from FICS traps to create luminescence.

4.4. Smart materials with dual role of Bi^{3+} in trapping both electrons and holes for X-ray imaging, anti-counterfeiting, and non-real-time force sensing

We propose that the $LiScGeO_4$ family of compounds can be designed as smart materials by using the dual role of Bi^{3+} in trapping both electrons and holes. Fig. 3(j) and (k) show that a Bi^{3+} negative quenching luminescence phosphor can be realized in $LiScGeO_4{:}0.005Bi^{3+}$ by using the compensation effect of thermally stimulated electron liberation from Bi^{2+} as evidenced in Fig. 5(a) until 5(g). Since the Bi^{2+} TL glow band is located below RT, the $LiScGeO_4{:}0.005Bi^{3+}$ can be utilized as an indicator to monitor extreme conditions, for instance in cryopreservation of biological samples like vaccines at -90 °C [84–86]. This is illustrated in Fig. 10.

Figs. 1, 2(e), 2(f), and S23 predict that wide range of UVA to infrared afterglow can be realized by using Bi^{3+} as a hole trapping and recombination center, and using the energy transfer processes from Bi^{3+} to Tb^{3+}, Dy^{3+}, or Cr^{3+}. This prediction is evidenced in the $LiScGeO_4$ family of compounds in Fig. 4. The wide range of emission tailorable afterglow, special Bi^{3+} UVA afterglow, and white afterglow have potential applications for advanced anti-counterfeiting, information encryption, and display as demonstrated in Figs. 8 and 9.

Fig. 6(a) shows that the TL intensity of $LiScGeO_4{:}0.003Bi^{3+}$, $0.005Tb^{3+}$ linearly increases with increasing X-ray exposure time. It has good stability after exposure to water in Fig. 6(k). It also has a weak TL fading characteristic in Fig. 6(g). The stored charged carriers in traps can be optically stimulated by wide range of 365 nm to 850 nm infrared laser beam in Figs. 6(i), 6(j), S17, and S18. These results collectively indicate that the Bi^{3+} co-doped $LiScGeO_4$ family of compounds can be used as potential dosimeters for advanced information encryption, storage, and readout, for example in the X-ray imaging application to inspect the internal structure of opaque objects in Fig. 11. Fig. 7(a) until 7(e) show

that the amount of stored charge carriers linearly increases with increasing the grinding duration. The Bi^{3+} co-doped $LiScGeO_4$ family of compounds also have potential use for special non-real-time force storage and sensing application.

5. Conclusions

In this work, the valence state change between Bi^{2+}, Bi^{3+}, and Bi^{4+}, and dual role of Bi^{3+} in trapping electrons and holes have been studied have been studied in the $LiScGeO_4$ family of compounds by utilizing the VRBE diagram, spectroscopy, and thermoluminescence. As evidenced by photoluminescence excitation and emission spectra after being illuminated by 254 or 365 nm with different duration in Fig. 3(e) until (g), the valence change of $Bi^{3+} \rightarrow Bi^{4+}$ is revealed in $LiScGeO_4$:0.003Bi^{3+} and $LiSc_{0.25}Lu_{0.75}GeO_4$:0.005$Bi^{3+}$. Upon Bi^{3+} D-band excitation, electrons are excited from the Bi^{3+} $^1S_0$ ground state to electron traps, forming Bi^{4+}. Reversed valence change from Bi^{4+} to Bi^{3+} is revealed. During 365 nm UV-light illumination, electrons are released from traps to recombine with holes trapped at Bi^{4+}, finally yielding Bi^{3+}. In Fig. 5(b) until 5 (g), a TL band peaked at ~266 K is observed in the range from 200 to ~300 K at β=1 K/s. It is assigned to the electron liberation from Bi^{2+} to recombine with holes captured at Bi^{4+}, Tb^{4+}, or Pr^{4+} in Bi^{3+} or/and Ln^{3+} doped $LiScGeO_4$ and $LiLuGeO_4$. Based on this result, the VRBE in the Bi^{2+} $^2P_{1/2}$ ground state is experimentally determined to be about -3.35 eV for $LiScGeO_4$ and $LiLuGeO_4$. Proof-of-concept Bi^{3+} negative quenching luminescence is demonstrated by using electron liberation from Bi^{2+}.

Particularly, a new force induced charge carrier storage (FICS) phenomenon appears in Bi^{3+} doped $LiScGeO_4$ family of compounds. The stored charge carriers created by the FICS effect can be liberated by wide range of 365 to 656 nm red laser. The FICS effect has promising use in non-real-time force storage and sensing application. Wide range of emission tailorable afterglow, unique Bi^{3+} UVA afterglow, and white afterglow have been realized by using Bi^{3+} as a hole trapping, recombination center, and energy transfer from Bi^{3+} to Tb^{3+}, Pr^{3+}, Dy^{3+}, or Cr^{3+}. Proof-of-concept advanced anti-counterfeiting, information encryption, and X-ray imaging have been demonstrated by using the developed Bi^{3+}-doped $LiScGeO_4$ family of compounds. This work not only develops smart storage phosphors by using the dual role of Bi^{3+} in trapping electrons and holes, but more importantly unravels the valence change between Bi^{2+}, Bi^{3+}, or Bi^{4+} and how it can affect the trapping and release of charge carriers with thermal, optical, or mechanical excitation. This work then can accelerate the discovery and development of Bi^{3+} based smart materials for various applications.

CRediT authorship contribution statement

Tianshuai Lyu: Conceptualization, Funding acquisition, Investigation, Writing – original draft, Writing – review & editing. **Pieter Dorenbos:** Formal analysis, Writing – review & editing. **Zhanhua Wei:** Resources.

Declaration of competing interest

The authors declare that they have no known competing financial interests or personal relationships that could have appeared to influence the work reported in this paper.

Acknowledgements

Supplementary materials

Supplementary material associated with this article can be found, in the online version, at doi:10.1016/j.actamat.2024.119953.

References

[1] Y. Zhuang, R.J. Xie, Mechanoluminescence rebrightening the prospects of stress sensing: a review, Adv. Mater. 33 (50) (2021) 2005925.

[2] S. Zhou, Y. Cheng, J. Xu, H. Lin, W. Liang, Y. Wang, Design of ratiometric dual-emitting mechanoluminescence: lanthanide/transition-metal combination strategy, Laser Photonics Rev. 16 (5) (2022) 2100666.

[3] P. Xiong, B. Huang, D. Peng, B. Viana, M. Peng, Z. Ma, Self-recoverable mechanically induced instant luminescence from Cr^{3+}-doped $LiGa_5O_8$, Adv. Funct. Mater. 31 (19) (2021) 2010685.

[4] T. Lyu, P. Dorenbos, P. Xiong, Z. Wei, $LiTaO_3$:Bi^{3+}, Tb^{3+}, Ga^{3+}, Ge^{4+}: a Smart perovskite with high charge carrier storage capacity for X-ray imaging, stress sensing, and non-real-time recording, Adv. Funct. Mater. 32 (39) (2022) 2206024.

[5] P. Shao, P. Xiong, Y. Xiao, Q. Chen, Y. Sun, N. Yan, D. Chen, Z. Yang, Novel spectral band: ultraviolet A mechanoluminescence from Bi^{3+}-doped $LiYGeO_4$, J. Mater. Chem. C 10 (44) (2022) 16670–16678.

[6] P. Shao, P. Xiong, Y. Xiao, Q. Chen, Y. Xiao, Y. Sun, D. Chen, Z. Yang, Tunable and enhanced mechanoluminescence in $LiYGeO_4$:Tb^{3+} via $Bi^{3+} \rightarrow Tb^{3+}$ energy transfer, J. Mater. Chem. C 11 (6) (2023) 2120–2128.

[7] S. Wu, B. Xiao, D. Jiang, Y. Xiao, P. Shao, Z. Zhou, Y. Wang, P. Xiong, Realizing near infrared mechanoluminescence switch in LAGO:Cr based on oxygen vacancy, Small. n/a (n/a) (2024) 2309034, https://doi.org/10.1002/smll.202309034.

[8] W. Wang, S. Wang, Y. Gu, J. Zhou, J. Zhang, Contact-separation-induced self-recoverable mechanoluminescence of CaF_2:Tb^{3+}/PDMS elastomer, Nat. Commun. 15 (1) (2024) 2014.

[9] N. Lin, J. Wang, Z. Xiao, R. Tan, Y. Zhang, S. Xu, G. Bai, Stimuli-responsive lanthanide activated piezoelectric $LiNbO_3$ microcrystals for multimode luminescence and optical sensing applications, Laser Photonics Rev. n/a (n/a) (2024) 2301352, https://doi.org/10.1002/lpor.202301352.

[10] T. Lyu, P. Dorenbos, Z. Wei, Versatile and high-performance $LiTaO_3$:Tb^{3+}, Gd^{3+} perovskite for multimode anti-counterfeiting, flexible X-ray imaging, continuous stress sensing, and non-real-time recording, Laser Photonics Rev. 17 (11) (2023) 2300323.

[11] S. Liu, Y. Zheng, D. Peng, J. Zhao, Z. Song, Q. Liu, Near-infrared mechanoluminescence of Cr^{3+} doped gallate spinel and magnetoplumbite smart materials, Adv. Funct. Mater. 33 (3) (2023) 2209275.

[12] C. Chen, Y. Zhuang, X. Li, F. Lin, D. Peng, D. Tu, A. Xie, R.J. Xie, Achieving remote stress and temperature dual-modal imaging by double-lanthanide-activated mechanoluminescent materials, Adv. Funct. Mater. 31 (25) (2021) 2101567.

[13] X. Yang, Y. Cheng, J. Xu, H. Lin, Y. Wang, Stress sensing by ratiometric mechanoluminescence: a strategy based on structural probe, Laser Photonics Rev. 16 (11) (2022) 2200365.

[14] T. Zheng, M. Runowski, I.R. Martín, K. Soler-Carracedo, L. Peng, M. Skwierczyńska, M. Sójka, J. Barzowska, S. Mahlik, H. Hemmerich, F. Rivera-López, P. Kulpiński, V. Lavín, D. Alonso, D. Peng, Mechanoluminescence and photoluminescence heterojunction for superior multi-mode sensing platform of friction, force, pressure and temperature in fibers and 3D-printed polymers, Adv. Mater. 35 (40) (2023) 2304140.

[15] Z. Liu, X. Yu, Q. Peng, X. Zhu, J. Xiao, J. Xu, S. Jiang, J. Qiu, X. Xu, NIR mechanoluminescence from Cr^{3+} activated $Y_3Al_5O_{12}$ with intense zero photon line, Adv. Funct. Mater. 33 (27) (2023) 2214497.

[16] L. Li, C. Cai, X. Lv, X. Shi, D. Peng, J. Qiu, Y. Yang, Stress-Triggered Mechanoluminescence in ZnO-Based Heterojunction for Flexible and Stretchable Mechano-Optics, Adv. Funct. Mater. 33 (32) (2023) 2301372.

[17] C. Chen, Z. Lin, H. Huang, X. Pan, T.L. Zhou, H. Luo, L. Jin, D. Peng, J. Xu, Y. Zhuang, R.J. Xie, Revealing the intrinsic decay of mechanoluminescence for achieving ultrafast-response stress sensing, Adv. Funct. Mater. 33 (46) (2023) 2304917.

[18] Y. Zhuang, X. Li, F. Lin, C. Chen, Z. Wu, H. Luo, L. Jin, R.J. Xie, Visualizing dynamic mechanical actions with high sensitivity and high resolution by near-distance mechanoluminescence imaging, Adv. Mater. 34 (36) (2022) 2202864.

[19] R.R. Petit, S.E. Michels, A. Feng, P.F. Smet, Adding memory to pressure-sensitive phosphors, Light Sci. Appl. 8 (1) (2019) 124.

[20] Y. Zhuang, D. Tu, C. Chen, L. Wang, H. Zhang, H. Xue, C. Yuan, G. Chen, C. Pan, L. Dai, R.J. Xie, Force-induced charge carrier storage: a new route for stress recording, Light Sci. Appl. 9 (1) (2020) 182.

[21] S. Liu, R. Yang, H. Cai, Y. Zhuang, Z. Song, L. Ning, Q. Liu, Electron tunneling charging upon sunlight for near-infrared persistent luminescence, Laser Photonics Rev. 17 (5) (2023) 2200999.

[22] L. Liang, J. Chen, K. Shao, X. Qin, Z. Pan, X. Liu, Controlling persistent luminescence in nanocrystalline phosphors, Nat. Mater. 22 (3) (2023) 289–304.

[23] A. Dobrowolska, A.J.J. Bos, P. Dorenbos, High charge carrier storage capacity in lithium lutetium silicate doped with cerium and thulium, Phys. Status Solidi (RRL) Rapid Res. Lett. 13 (3) (2019) 1800502.

[24] L. Yuan, Y. Jin, Y. Su, H. Wu, Y. Hu, S. Yang, Optically stimulated luminescence phosphors: principles, applications, and prospects, Laser Photonics Rev. 14 (12) (2020) 2000123.

[25] P. Leblans, D. Vandenbroucke, P. Willems, Storage phosphors for medical imaging, Materials 4 (6) (2011) 1034–1086.

[26] Z. Yang, J. Hu, D. Van der Heggen, M. Jiao, A. Feng, H. Vrielinck, P.F. Smet, D. Poelman, A versatile photochromic description enabling detection of X-ray, ultraviolet, and visible photons, Laser Photonics Rev. 17 (5) (2023) 2200809.

[27] C. Liao, H. Wu, H. Wu, L. Zhang, G.H. Pan, Z. Hao, F. Liu, X.J. Wang, J. Zhang, Electron trapping optical storage using a single-wavelength light source for both information write-in and read-out, Laser Photonics Rev. 17 (8) (2023) 2300016.

[28] L. Wang, C. Wang, Y. Chen, Y. Jiang, L. Chen, J. Xu, B. Qu, H.T. Hintzen, Red-emitting $SrGa_2O_4$:Cu^{2+} phosphor with super-long persistent luminescence, Chem. Mater. 34 (22) (2022) 10068–10076.

[29] T. Lyu, P. Dorenbos, Z. Wei, Designing $LiTaO_3$:Ln^{3+}, Eu^{3+} (Ln=Tb or Pr) perovskite dosimeter with excellent charge carrier storage capacity and stability for anti-counterfeiting and flexible X-ray imaging, Chem. Eng. J. 461 (2023) 141685.

[30] T. Lyu, P. Dorenbos, C. Li, S. Li, J. Xu, Z. Wei, Unraveling electron liberation from Bi^{2+} for designing Bi^{3+}-based afterglow phosphor for anti-counterfeiting and flexible X-ray imaging, Chem. Eng. J. 435 (2022) 135038.

[31] T. Lyu, How to rational design and explore afterglow and storage phosphors by using vacuum referred binding energy (VRBE) diagram, Chin. J. Lumin. 43 (9) (2022) 1413–1427.

[32] T. Lyu, P. Dorenbos, Towards information storage by designing both electron and hole detrapping processes in bismuth and lanthanide-doped $LiRE(Si,Ge)O_4$ (RE=Y, Lu) with high charge carrier storage capacity, Chem. Eng. J. 400 (2020) 124776.

[33] T. Lyu, P. Dorenbos, Designing thermally stimulated 1.06 μm Nd^{3+} emission for the second bio-imaging window demonstrated by energy transfer from Bi^{3+} in La-, Gd-, Y-, and $LuPO_4$, Chem. Eng. J. 372 (2019) 978–991.

[34] P. Dorenbos, Modeling the chemical shift of lanthanide 4f electron binding energies, Phys. Rev. B 85 (16) (2012) 165107.

[35] P. Dorenbos, Electronic structure engineering of lanthanide activated materials, J. Mater. Chem. 22 (42) (2012) 22344–22349.

[36] P. Dorenbos, The nephelauxetic effect on the electron binding energy in the $4f^q$ ground state of lanthanides in compounds, J. Lumin. 214 (2019) 116536.

[37] T. Lyu, P. Dorenbos, Charge carrier trapping management in Bi^{3+} and lanthanides doped Li(Sc,Lu)GeO_4 for x-ray imaging, anti-counterfeiting, and force recording, Appl. Phys. Rev. 11 (1) (2024) 011415.

[38] Y. Liu, B. Lei, C. Shi, Luminescent Properties of a White Afterglow Phosphor $CdSiO_3$:Dy^{3+}, Chem. Mater. 17 (8) (2005) 2108–2113.

[39] X. Wang, Y. Chen, F. Liu, Solar-blind ultraviolet-C persistent luminescence phosphors, Nat. Commun. 11 (1) (2020) 2040.

[40] L. Yang, S. Gai, H. Ding, D. Yang, L. Feng, P. Yang, Recent progress in inorganic afterglow materials: mechanisms, persistent luminescent properties, modulating methods, and bioimaging applications, Adv. Opt. Mater. 11 (11) (2023) 2202382.

[41] Y. Tang, M. Deng, M. Wang, X. Liu, Z. Zhou, J. Wang, Q. Liu, Bismuth-activated persistent phosphors, Adv. Opt. Mater. 11 (2) (2023) 2201827.

[42] R. Cao, T. Huang, J. Nie, L. Zhang, Y. Chen, L. Li, B. Lan, J. Wang, Energy transfer and tunable-color luminescence properties of a single-phase $CaSrNb_2O_7$:Sm^{3+}, Bi^{3+}, J. Mol. Struct. 1297 (2024) 136962.

[43] R. Cao, T. Chen, Y. Ren, C. Liao, Z. Luo, Y. Ye, Y. Guo, Tunable emission of $LiCa_3MgV_3O_{12}$:Bi^{3+} via energy transfer and changing excitation wavelength, Mater. Res. Bull. 111 (2019) 87–92.

[44] S. Saikia, A. Ghosh, A. Nag, Broad dual emission by codoping Cr^{3+} (d-d) and Bi^{3+} (s-p) in $Cs_2Ag_{0.6}Na_{0.4}InCl_6$ double perovskite, Angew. Chem. Int. Ed. 62 (33) (2023) e202307689.

[45] X. Li, H. Lin, S. Lin, P. Li, P. Wang, J. Xu, Y. Cheng, Q. Zhang, Y. Wang, Rare-earth-ion doped $Bi_{1.5}ZnNb_{1.5}O_7$ Photochromics: a fast self-recoverable optical storage medium for dynamic anti-counterfeiting with high security, Laser Photonics Rev. 17 (5) (2023) 2200734.

[46] Y. Zhang, D. Chen, W. Wang, S. Yan, J. Liu, Y. Liang, Long-lasting ultraviolet-A persistent luminescence and photostimulated persistent luminescence in Bi^{3+}-doped $LiScGeO_4$ phosphor, Inorg. Chem. Front. 7 (17) (2020) 3063–3071.

[47] S. Miao, Y. Liang, D. Chen, S. Yan, J. Liu, W. Wang, J. Bi, Enabling narrowband cyan photoluminescence and long-lasting ultraviolet-A persistent luminescence in Bi^{3+} single-doped $Sr_3Sc_2Ge_3O_{12}$ phosphors by selective site occupation, J. Mater. Chem. C 10 (38) (2022) 14211–14219.

[48] J. Jia, X. Gao, G. Zou, Alkaline-earth-metal-ions blending enhanced self-activated and Bi^{3+}-activated mechanoluminescence from $Ca_{1-x}Ba_xZnOS$, Adv. Funct. Mater. 32 (46) (2022) 2207881.

[49] Z. Qiao, C. Wang, C. Heng, W. Jin, L. Ning, Exploring intrinsic electron-trapping centers for persistent luminescence in Bi^{3+}-Doped $LiREGeO_4$ (RE=Y, Sc, Lu): mechanistic origin from first-principles calculations, Inorg. Chem. 60 (21) (2021) 16604–16613.

[50] Z. Zhou, P. Xiong, H. Liu, M. Peng, Ultraviolet-A persistent luminescence of a Bi^{3+}-Activated $LiScGeO_4$ material, Inorg. Chem. 59 (17) (2020) 12920–12927.

[51] T. Lyu, P. Dorenbos, Vacuum-referred binding energies of bismuth and lanthanide levels in $ATaO_3$ (A=Li, Na, K) Perovskite: toward designing energy storage phosphor for anti-counterfeiting, X-ray imaging, and mechanoluminescence, Laser Photonics Rev. 16 (10) (2022) 2200304.

[52] T. Lyu, P. Dorenbos, C. Li, Z. Wei, Wide range X-ray to infrared photon detection and energy storage in $LiTaO_3$:Bi^{3+}, Dy^{3+} perovskite, Laser Photonics Rev. 16 (9) (2022) 2200055.

[53] H. Yang, X. Chen, Y. Chu, C. Sun, H. Lu, M. Yuan, Y. Zhang, G. Long, L. Zhang, X. Li, A universal hydrochloric acid-assistant powder-to-powder strategy for quick and mass preparation of lead-free perovskite microcrystals, Light Sci. Appl. 12 (1) (2023) 75.

[54] M. Jin, W. Zheng, Z. Gong, P. Huang, R. Li, J. Xu, X. Cheng, W. Zhang, X. Chen, Unraveling the triplet excited-state dynamics of Bi^{3+} in vacancy-ordered double perovskite Cs_2SnCl_6 nanocrystals, Nano Res. 15 (7) (2022) 6422–6429.

[55] M. Szymczak, M. Runowski, V. Lavín, L. Marciniak, Highly pressure-sensitive, temperature independent luminescence ratiometric manometer based on MgO:Cr^{3+} Nanoparticles, Laser Photonics Rev. 17 (4) (2023) 2200801.

[56] F. Zhao, Z. Song, Q. Liu, Advances in chromium-activated phosphors for near-infrared light sources, Laser Photonics Rev. 16 (11) (2022) 2200380.

[57] T. Lyu, P. Dorenbos, Bi^{3+} acting both as an electron and as a hole trap in La-, Y-, and $LuPO_4$, J. Mater. Chem. C 6 (23) (2018) 6240–6249.

[58] T. Lyu, P. Dorenbos, Vacuum-referred binding energies of bismuth and lanthanide levels in $ARE(Si,Ge)O_4$ (A=Li, Na; RE=Y, Lu): toward designing charge-carrier-trapping processes for energy storage, Chem. Mater. 32 (3) (2020) 1192–1209.

[59] P. Huang, Z. Wen, Y. Yu, J. Xiao, Z. Wei, T. Lyu, High charge carrier storage capacity and wide range X-rays to infrared photon sensing in $LiLuGeO_4$:Bi^{3+}, Ln^{3+} (Ln=Pr, Tb, or Dy) for anti-counterfeiting and information storage applications, Mater. Chem. Front. 7 (1) (2023) 168–182.

[60] Q. Liu, Z.Y. Feng, H. Li, Q. Zhao, N. Shirahata, Y. Kuroiwa, C. Moriyoshi, C. K. Duan, H.T. Sun, Non-rare-earth UVC persistent phosphors enabled by bismuth doping, Adv. Opt. Mater. 9 (8) (2021) 2002065.

[61] S. Gu, H. Guo, Q. Shi, L. Wang, C.e. Cui, Y. Cui, P. Huang, Sunlight-activated orange persistent luminescence from bi-doped $SrBaZn_2Ga_2O_7$ for warm-color optical applications, Inorg. Chem. 60 (24) (2021) 19233–19241.

[62] D. Liu, X. yun, P. dang, H. lian, M. shang, G. li, J. lin, Yellow/orange-emitting $ABZn_2Ga_2O_7$:Bi^{3+}(A=Ca, Sr; B=Ba, Sr) phosphors: optical temperature sensing and white light-emitting diode applications, Chem. Mater. 32 (7) (2020) 3065–3077.

[63] W. Hoogenstraaten, Electron traps in zinc sulphide phosphors, Philips Res. Rep. 13 (1958) 515–693.

[64] R. Chen, S.A.A. Winer, Effects of various heating rates on glow curves, J. Appl. Phys. 41 (13) (2003) 5227–5232.

[65] D. Kulesza, A.J.J. Bos, E. Zych, The effect of temperature and excitation energy of the high- and low-spin 4f→5d transitions on charging of traps in Lu_2O_3:Tb, M (M = Ti, Hf), Acta Mater. 231 (2022) 117852.

[66] J. Ueda, P. Dorenbos, A.J.J. Bos, K. Kuroishi, S. Tanabe, Control of electron transfer between Ce^{3+} and Cr^{3+} in the $Y_3Al_{5-x}Ga_xO_{12}$ host via conduction band engineering, J. Mater. Chem. C 3 (22) (2015) 5642–5651.

[67] Z. Zhou, X. Wang, X. Yi, H. Ming, Z. Ma, M. Peng, Rechargeable and sunlight-activated $Sr_3Y_2Ge_3O_{12}$:Bi^{3+} UV–Visible-NIR persistent luminescence material for night-vision signage and optical information storage, Chem. Eng. J. 421 (2021) 127820.

[68] Y.L. Yang, T. Li, F. Guo, J.Y. Yuan, C.H. Zhang, Y. Zhou, Q.L. Li, D.Y. Wan, J. T. Zhao, Z.J. Zhang, Multiple color emission of mechanoluminescence and photoluminescence from $SrZnSO$:Bi^{3+} for multimode anticounterfeiting, Inorg. Chem. 61 (10) (2022) 4302–4311.

[69] P. Liu, Y. Zhang, B. Li, L. Han, Y. Xu, Trap depth engineering in $MgGa_2O_4$:Bi^{3+} for muticolor dynamic anti-counterfeiting, encryption and optical temperature sensing applications, Chem. Eng. J. 437 (2022) 135389.

[70] R.H.P. Awater, P. Dorenbos, Towards a general concentration quenching model of Bi^{3+} luminescence, J. Lumin. 188 (2017) 487–489.

[71] T. Lyu, P. Dorenbos, Charge carrier trapping processes in lanthanide doped $LaPO_4$, $GdPO_4$, YPO_4, and $LuPO_4$, J. Mater. Chem. C 6 (2) (2018) 369–379.

[72] J. Kong, W. Zheng, Y. Liu, R. Li, E. Ma, H. Zhu, X. Chen, Persistent luminescence from Eu^{3+} in SnO_2 nanoparticles, Nanoscale 7 (25) (2015) 11048–11054.

[73] Y.H. Kim, P. Arunkumar, B.Y. Kim, S. Unithrattil, E. Kim, S.H. Moon, J.Y. Hyun, K. H. Kim, D. Lee, J.S. Lee, W.B. Im, A zero-thermal-quenching phosphor, Nat. Mater. 16 (5) (2017) 543–550.

[74] X. Fan, W. Chen, S. Xin, Z. Liu, M. Zhou, X. Yu, D. Zhou, X. Xu, J. Qiu, Achieving long-term zero-thermal-quenching with the assistance of carriers from deep traps, J. Mater. Chem. C 6 (12) (2018) 2978–2982.

[75] D. Wen, H. Liu, Z. Ma, L. Zhou, J. Li, Y. Guo, Q. Zeng, P.A. Tanner, M. Wu, Improved thermal and chemical stability of oxynitride phosphor from facile chemical synthesis for cornering lights, Angew. Chem. Int. Ed. 62 (35) (2023) e202307868.

[76] A. Dobrowolska, A.J.J. Bos, P. Dorenbos, Charge carrier storage properties and the vacuum referred binding energy scheme for $Li_2BaP_2O_7$:Ln (Ln=Ce, Eu, Tb, Yb), J. Lumin. 170 (2016) 497–504.

[77] Z. Ma, Y. Han, Y. Bai, B. Liu, Z. Wang, Near-ultraviolet and deep red dual-band mechanoluminescence for color manipulation and biomechanics detection, Chem. Eng. J. 456 (2023) 141122.

[78] Y. Bai, F. Wang, L. Zhang, D. Wang, Y. Liang, S. Yang, Z. Wang, Interfacial triboelectrification-modulated self-recoverable and thermally stable mechanoluminescence in mixed-anion compounds, Nano Energy 96 (2022) 107075.

[79] Z. Ma, J. Zhou, J. Zhang, S. Zeng, H. Zhou, A.T. Smith, W. Wang, L. Sun, Z. Wang, Mechanics-induced triple-mode anticounterfeiting and moving tactile sensing by simultaneously utilizing instantaneous and persistent mechanoluminescence, Mater. Horiz. 6 (10) (2019) 2003–2008.

[80] Z. Huang, B. Chen, B. Ren, D. Tu, Z. Wang, C. Wang, Y. Zheng, X. Li, D. Wang, Z. Ren, S. Qu, Z. Chen, C. Xu, Y. Fu, D. Peng, Smart mechanoluminescent phosphors: a review of strontium-aluminate-based materials, properties, and their advanced application technologies, Adv. Sci. 10 (3) (2023) 2204925.

[81] D. Tu, C.N. Xu, A. Yoshida, M. Fujihala, J. Hirotsu, X.G. Zheng, LiNbO$_3$:Pr^{3+}: a multipiezo material with simultaneous piezoelectricity and sensitive piezoluminescence, Adv. Mater. 29 (22) (2017) 1606914.

[82] C.N. Xu, T. Watanabe, M. Akiyama, X.G. Zheng, Direct view of stress distribution in solid by mechanoluminescence, Appl. Phys. Lett. 74 (17) (1999) 2414–2416.

[83] J.C. Zhang, X. Wang, G. Marriott, C.N. Xu, Trap-controlled mechanoluminescent materials, Prog. Mater. Sci. 103 (2019) 678–742.

[84] Y. Song, J. Du, R. Yang, C. Lin, W. Chen, Z. Wu, H. Lin, X. Chen, Y. Zhuang, R. J. Xie, Recyclable time–temperature indicator enabled by light storage in particles, Adv. Opt. Mater. 11 (8) (2023) 2202654.

[85] J. Du, D. Poelman, Identifying near-infrared persistent luminescence in Cr^{3+}-doped magnesium gallogermanates featuring afterglow emission at extremely low temperature, Adv. Opt. Mater. 8 (6) (2020) 1901848.

[86] Y. Liu, H. Zhang, Z. Liu, Y. Cai, C. Wang, H. Lv, X. Zhu, C. Wang, X. Yu, J. Qiu, H. Ma, L. Zhao, X. Xu, Identifying and utilizing optical properties in the CaSrNb$_2$O$_7$:Pr^{3+} phosphor at low temperature, J. Mater. Chem. C 10 (9) (2022) 3547–3552.